Experimental and Numerical Investigation of Insulated Bayonet Freeze Tubes for Artificial Ground Freezing

Aurelien Nie-Rouquette
Mining and Materials Engineering
McGill University, Montreal

Submitted: April 2018

A thesis submitted to McGill University in partial fulfillment of the requirements of the degree of Master of Engineering

Abstract

Insulated bayonet freeze pipes were investigate using experimental and numerical models. A numerical model for the air insulation was built and validated against literature experiments. The analysis showed that the boundary condition on the end caps can have important effects on the natural convection's process. A laboratory-scale model was built and its readings were shown to be repeatable. Experimental results were compared to a numerical model for frozen and unfrozen regimes. The active and transition zones were easily validated. However, the passive zone showed significant difference. A Nusselt number of around 10 would be required to make the data fit, which is unrealistic. Further research is recommended. The passive zone's numerical model is extended to test the influence of eccentricity on heat transfer. As long as there is no contact, the effects are minimal. However, a fully eccentric passive zone increases the heat transfer rate by a whole order of magnitude, and is thus to be avoided at all cost.

Acknowledgments

If this thesis was a ship navigating using the stars, then my supervisor Agus Sasmito was the one that kept reminding me to look at the sky. His help and guidance have been instrumental in the shaping of this research. I have been very fortunate to be his student. I also wish to thank my lab mates who have made the writing process bearable if not enjoyable. In particular, I am grateful for Mahmoud Alzoubi's help. The regular discussions have helped tremendously over the years. CAMECO also deserves a mention here (and a particular shout out to Marty Wacker). Their feedback based on their operations have always been relevant. This research would not have been possible without the help of Thierry Lafrance from Mëkanic and John Brohan. Their contribution to the construction fo the experiment was indispensable. Finally, I would like to thank my parents and brothers for pushing me to do this Masters Thesis. Their continued support is appreciated. Thanks to Max for making sure the language was understandable.

This research was in part funded by Areva, Cameco, Canadian Foundation for Innovation (CFI), Compute Canada, Mëkanic, Natural Sciences and Engineering Research Council (NSERC), Newmans Geotechnique and Ultra Deep Mining Network (UDMN).

Contents

1 Introduction **8**
- 1.1 Background . . . 8
  - 1.1.1 Artificial Ground Freezing . . . 8
  - 1.1.2 AGF in Uranium Mine . . . 10
- 1.2 Issues and Objectives . . . 10
- 1.3 Outline of Thesis . . . 12

2 Literature Review **13**
- 2.1 Organization . . . 13
- 2.2 Freezing in Porous Ground . . . 13
  - 2.2.1 Thermal Properties of soils . . . 14
  - 2.2.2 Modeling of Freezing in Porous Media . . . 14
- 2.3 State of the Art for AGF . . . 16
  - 2.3.1 Experimental Studies . . . 16
  - 2.3.2 Mathematical Models . . . 17
- 2.4 Natural Convection in Annulus . . . 18

3 Experimental Setup **20**
- 3.1 Introduction . . . 20
- 3.2 Physical Setup . . . 20
  - 3.2.1 Overview . . . 20
  - 3.2.2 Tank and Sand . . . 21
  - 3.2.3 Insulated Bayonet Freezing Tube and Piping . . . 22
  - 3.2.4 Coolant, Chiller and Pump . . . 24
  - 3.2.5 Piping . . . 25
- 3.3 Measurement and control . . . 26
  - 3.3.1 Data Acquisition Instruments . . . 26
  - 3.3.2 Temperature . . . 27

3.3.3 Flow Rate . . . 28
3.3.4 Pressure . . . 30
3.4 Material Properties . . . 30
3.4.1 Measurement . . . 30
3.5 Repeatability of Results . . . 33

4 Numerical Model Development and Validation 37
4.1 Natural Convection in Closed Annulus . . . 37
4.1.1 Experimental Model . . . 37
4.1.2 Numerical Model . . . 39
4.1.3 Results and Validation . . . 40
4.2 AGF in Laboratory Environment . . . 43
4.2.1 Numerical Model . . . 43
4.2.2 Boundary Conditions . . . 43
4.2.3 Material Properties . . . 45
4.2.4 Equations . . . 45
4.3 Validation against Experiment . . . 47
4.3.1 Air Gap Validation for IBFT . . . 47
4.3.2 Unfrozen regime . . . 49
4.3.3 Frozen regime . . . 50

5 Investigation of Eccentricity 54
5.1 Numerical Model . . . 54
5.2 Results . . . 55
5.2.1 Modes of Heat Transfer . . . 55
5.2.2 Influence of Temperature . . . 57

6 Summary and Conclusion 58

List of Figures

1.1 Applicability of Geotechnical Processes according to Soil Types 9
1.2 Diagram of Bayonet Freeze Tubes 9
1.3 Geology of Cigar Lake Mine 11

3.1 Flowsheet of Insulated Bayonet Freeze Tube Setup 21
3.2 Whole experiment in lab setting 22
3.3 Cross-section showing instrumentation 23
3.4 Insulated bayonet freeze tube assembly 24
3.5 Nominal cooling capacity of the G50 Chiller 25
3.6 LabVIEW Environment for the experiment 26
3.7 Location of the Thermocouples on the Support and TC Naming Convention (Dimensions in inches) 27
3.8 3D model and picture of Support 28
3.9 Calibration Setup for Thermocouples 29
3.10 Sample Thermocouple Calibration Curve 30
3.11 Flowmeter and Connection Diagram 31
3.12 Measured Glycol Properties 32
3.13 XRD Pattern Matching for Dry Sand 34
3.14 Comparison of Flow Rate and Heat Gain between Experiments 34
3.15 Temperature of sand thermocouples close in Active Zone . . . 35
3.16 Temperature of sand thermocouples close in Transition Zone . 35
3.17 Temperature of sand thermocouples close in Passive Zone . . . 35
3.18 Comparison of Average Sand Temperature Readings 36

4.1 Schematics of Keyhani's experimental setup 38
4.2 Validation of Temperature Profile on Heater Rod. 41
4.3 Temperature and Velocity Profile in Annular Natural Convection 42
4.4 Zones and meshing of Simulation (selected regions) 44
4.5 Comparison of Analytical, Empirical [35] and Numerical Results 48

4.6 Inlet and Outlet Temperature in Unfrozen Conditions 49
4.7 Unfrozen Sand Temperatures in Active Zone 50
4.8 Unfrozen Sand Temperatures in Transition Zone 51
4.9 Unfrozen Sand Temperatures in Passive Zone 51
4.10 Inlet and Outlet Temperature in Frozen Conditions 52
4.11 Frozen Sand Temperatures in Active Zone 53
4.12 Frozen Sand Temperatures in Transition Zone 53
4.13 Frozen Sand Temperatures in Passive Zone 53

5.1 Geometry of Perfectly Concentric and Perfectly Eccentric IBFT 55
5.2 Modes of Heat Transfer in Concentric and Eccentric IBFT . . 56
5.3 Temperature Profile in Concentric and Eccentric Configurations 56
5.4 Effect of eccentricity at different temperatures 57

List of Tables

2.1 Summary of Freezing Experiments (Adapted from [28]) 17
2.2 Annular Flow Regimes 18
2.3 Heat Transfer Correlations for Natural Convection in Annulus 19

3.1 Experimental Thermo-Physical Properties of Glycol and Sand 33

4.1 Material Properties for Natural Convection 38

Chapter 1

Introduction

1.1 Background

1.1.1 Artificial Ground Freezing

One of the main technical challenges in Mining and geotechnical engineering is to design around the ground in which projects occur. In particular, weak and fractured ground can cause numerous safety and groundwater problems. Artificial Ground Freezing (AGF) is a technique that alleviates both of these problems by freezing the water in the frozen ground's pores. This creates an impermeable ice matrix that cements the ground particles which prevents groundwater flow and increases the bulk strength. The technique can be applied in almost any types of grounds, from the very fractures soils to competent rock formations (Figure 1.1).

The most common method for implementing AGF is via the use of bayonet freeze tubes. These heat exchangers are made of two concentric pipes, with the outer one being capped at the end (Figure 1.2). Coolant circulates, usually from the inner and flowing back through the annulus. This configuration can be installed within a single drill hole with relative ease and is very easy to assemble and maintain, although it is not a efficient type of heat exchanger.

Even with these significant advantages, AGF is usually not the first choice for ground support technique. The reason is simple: AGF is expensive. A great number of freeze holes are typically needed to make the technique reliable. Furthermore, AGF must operate unceasingly to prevent thawing and thus incurs continuous expenditures. Therefore AGF is mainly used

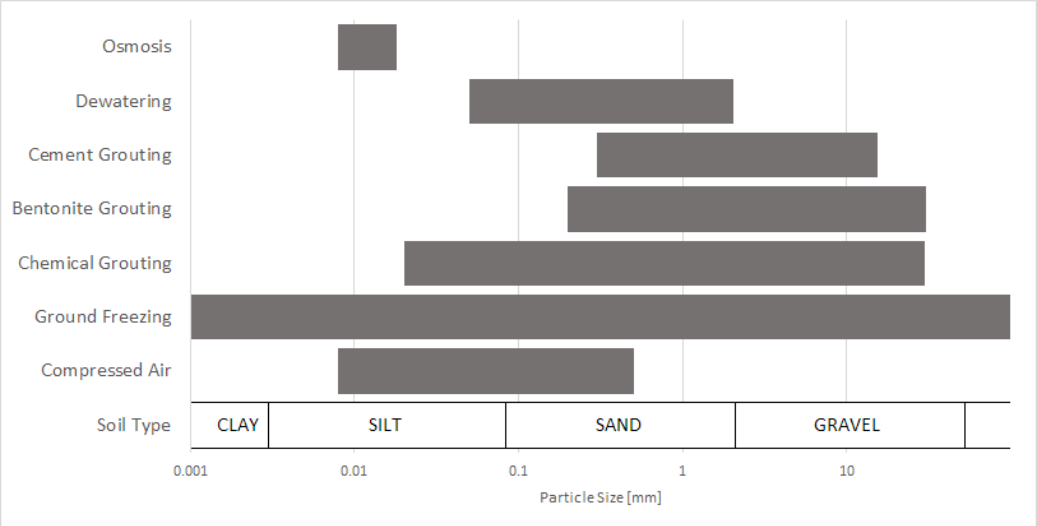

Figure 1.1: Applicability of Geotechnical Processes according to Soil Types (Adapted from [1])

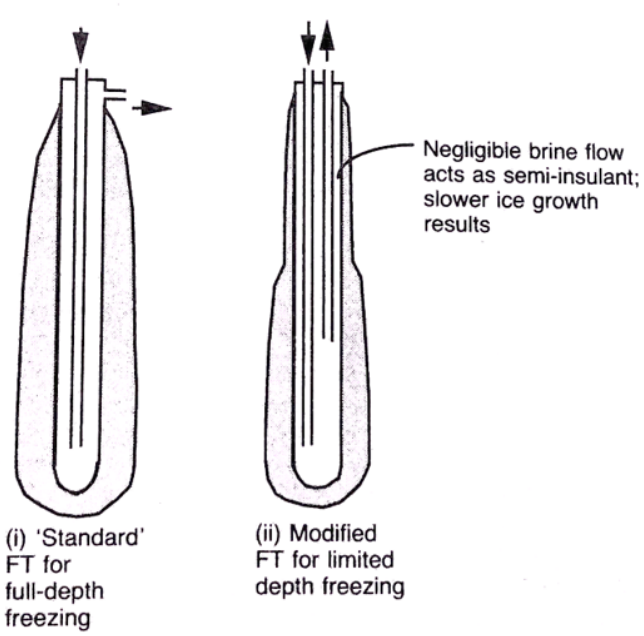

Figure 1.2: Diagram of Bayonet Freeze Tubes (From [1])

as temporary support before installing a permanent solution. For example, shaft sinking and tunneling will use AGF to create a temporary ice wall before and during the excavation, but will install a concrete lining after and let the ice wall thaw.

In rare cases, AGF is the only possible solution for groundwater control and support. For instance, the recent Fukushima disaster remediation plan uses AGF to quarantine the radiative run-off water from the reactor. [2] In the mining department, two Uranium operations come to mind: McArthur Lake and Cigar Lake mine, both operated by CAMECO. The application of AGF in this type of mining operation will th the focus of the thesis.

1.1.2 AGF in Uranium Mine

Two mining operations by CAMECO use AGF as a main groundwater control strategy: McArthur River and Cigar Lake. In both of these cases, the ore is located at depth in a highly fractured ground with high water pressure. The high water inflow in these areas would require massive pumping facilities. Furthermore, the water could be contaminated by radiation, which would cause environmental issues. Freezing elegantly solves these two problems.

McArthur River's orebody is adjacent to a competent hanging wall on the South. AGF creates a freeze wall that goes from tunnels in the freeze walls to the bedrock below to create an dry isolated ore zone. The ore can then be extracted from galleries under the orebody using high-pressured water jet. This was also the strategy employed in Cigar Lake originally. However, freeze wall failures in 2006 and 2008 caused some significant flooding and delays. To keep up with the schedule, the company decided to use bulk freezing from surface. Since the orebody is located at a depth of around 400m, this requires significant drilling. The sandstone and gneiss in Figure 1.3 is impermeable, and thus only a length of around 60m require active freezing. In other words, any AGF between the top of the deposit and surface is wasted energy. To reduce energy loss, CAMECO is using an air insulation to create a passive heat transfer zone. They have been using this method since 2014.

1.2 Issues and Objectives

Bayonet freeze tube have already been the topic of a number of studies. Insulated bayonet freeze tubes, on the other hand, has mostly been ignored.

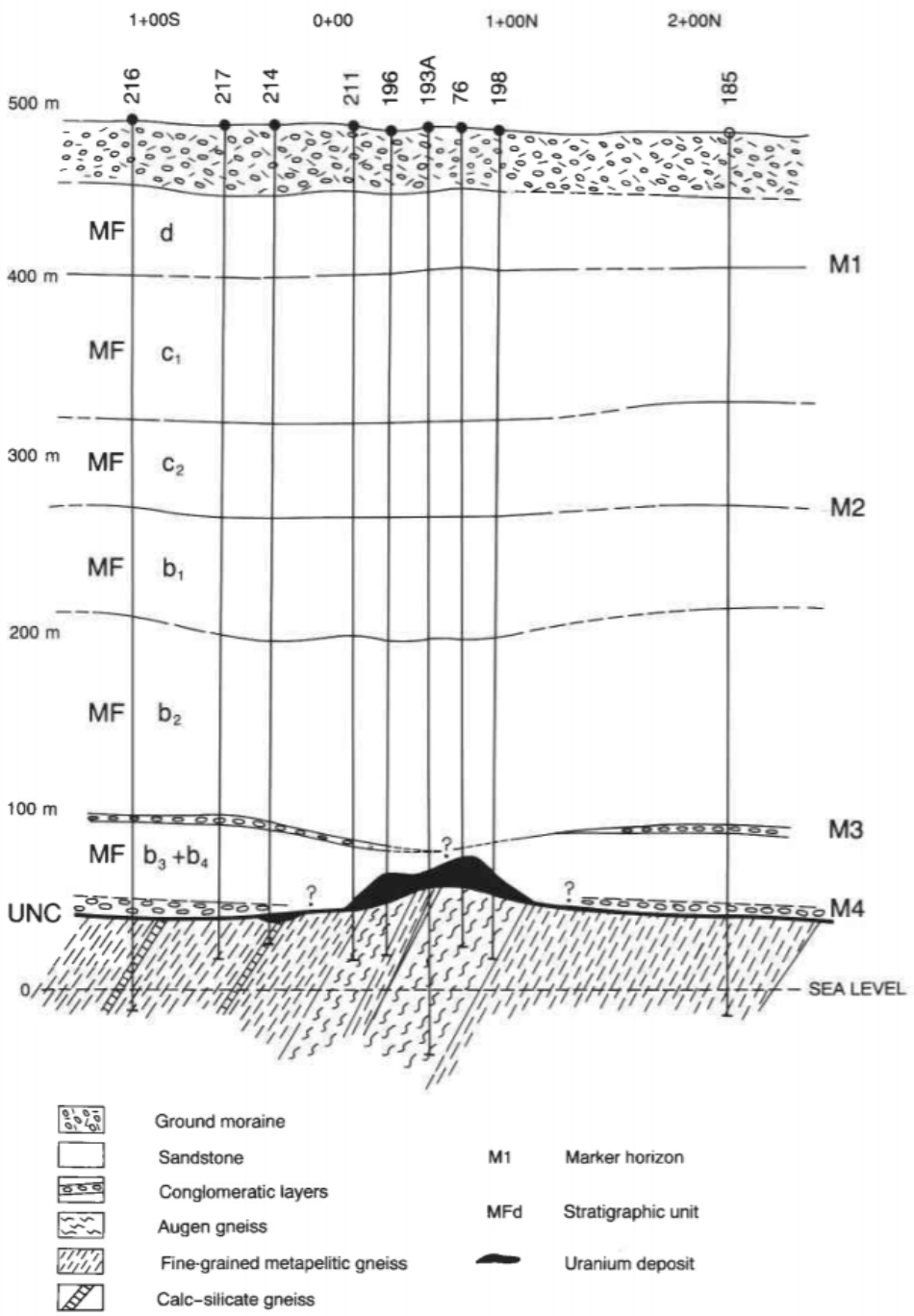

Figure 1.3: Geology of Cigar Lake Mine (From [3])

Field measurements have shown the insulation to be an effective way to decrease energy consumption. However, field conditions are quite variable and depend on a number of factors that can be difficult to measure and account for. In addition, field data is rarely published as it is private company information. We solve these issues by building a laboratory-scale AGF experiment to gather reliable data.

The next obstacle towards getting a better understanding and performance in IBFT is the lack of framework. Many numerical models exist for simple bayonet tubes, but none exist for IBFT. A numerical model will accelerate parametric studies and help understand the main principles of the heat transfer. This thesis will aim to create a model validated against the previously discussed experimental model and use this model to optimize AGF systems. Our hope is that the results of this research will help AGF operations freeze faster with less energy expenditure.

Even though one of the main goals of AGF is to strengthen the ground, this research will not aim to examine the effect of AGF on ground strength.

1.3 Outline of Thesis

The first section of the thesis describes the laboratory-scale AGF model and analyses the quality of results from this experiment. The following section presents a numerical model and validates it against experiments. Finally, the numerical model is extended to perform parametric studies on insulation dimensions and composition. Furthermore, the effect of eccentricity on heat transfer is investigated.

Chapter 2

Literature Review

2.1 Organization

This chapter describes the available literature relevant to this study. To understand how artificial ground freezing functions, it is imperative to first understand the mechanisms of heat transfer in soil. In particular, methods to derive bulk thermal conductivity for different soils will be described. The next portion will describe the current state of art for artificial ground freezing. Current best practices and recent research will be outlined. The latter includes experimental and numerical research, and field studies. Following it is a discussion on natural convection in a closed annulus. The many different correlations will be summarized to better understand the phenomenon.

The current research will discuss mainly thermal properties in AGF. As such, thermo-mechanical phenomena such as frost heaving and rock mass strengthening will be mostly ignored. I would recommend referring to [4] and [5] for such matters.

2.2 Freezing in Porous Ground

AGF models rely heavily on the current understanding of freezing in porous media. In fact, in most AGF situations, the ground itself is the limiting factor [6]. As such, a brief overview of the relevant topics of this extensive field will be presented.

2.2.1 Thermal Properties of soils

The first important point is the determination of the soil's bulk conductivity. This information is crucial in any model that models the ground as a two-phase region. Johansen makes a thorough examination of this topic [7] although it is quite dated. What follows is a short summary of some of the more widespread calculation techniques and more recent studies.

When ϕ is low, an arithmetic, geometric of harmonic mean may give good results, depending on the grain distribution [8]. For dispersed solids when the porosity is higher, an approach based on Maxwell's electric conductivity formula may be modified and used to great accuracy. Analytical and semi-analytical models have been refined by taking into account, grain shape [9], saturation degree [10] [11] and grain size distribution [12]. Coté and Konrad simplify this general equation by correlating some of these with field measurements such as dry and wet densities and mineral composition [13]

Fully empirical models have also been developed. For instance, Pei et al. demonstrate and validate a model based on multiple linear regression [14].

2.2.2 Modeling of Freezing in Porous Media

Freezing models in porous media fall in two broad categories depending on their purpose: Thermo-Hydraulic (TH) or Thermo-Hydro-Mechanical (THM) models; the main difference resides in the inclusion of ice pressure [15]. Civil engineers tend to rely more strongly on THM due to the prediction of stress and load-bearing capacity while soil scientists are more interested in the temperature and water content.

One of the earliest models can be attributed to de Vries in 1957 [9], based on moisture movement in pores from temperature gradient in unsaturated soils. Since then, a number of models have been produced. Li et al [16] provide a review of these different models and outline the differences between models.

- Complexity of the frozen soil model, in particular the treatment of the phase change
- Method for dealing with freeze-melting process
- Validation of the model and dataset used

Liu et al. [15] perform a similar literature review, but with a stronger focus on the theory behind the equation set used for each parameter. A review of possible options for each parameter is outlined below.

- Moisture movement can modeled by gravimetry, surface tension, temperature gradient or ice pressure
- Coupling between particles, liquid and solid phase is usually modeled using hydrodynamic or rigid ice model.
- Models can be fully analytical or semi-empirical
- The scale of the model's interactions (microscopic vs macroscopic)
- The water characteristic curve used in the model will affect the accuracy of the solution, although it depends on the soil.
- As discussed in Section 2.2.1, models with different bulk thermal conductivity will yield different predictions.
- Since solidification effectively decreases permeability, the treatment methodology will have an important impact on the results.
- Treatment of phase change as porosity-enthalpy, apparent specific heat or frozen front

Finally, Kurylyk [17] provides a review on the way different 1D and 3D freezing models treat the following equations. The methods of validation are also highlighted.

- Clapeyron equation
- Soil-water and soil-freezing curves
- hydraulic conductivity of partially frozen soil

2.3 State of the Art for AGF

AGF was first used in 1862, but was only patented in 1883 by Poetsch [1] and has since then been used in civil and mining operations around the globe. It is a popular technique for shaft sinking [18], tunneling [19] and underground water control in mining [20] . This technique is also used to control water contamination, such as at Fukushima, Japan[21], [2], and Giant Mine, North West Territories[22]. Furthermore, the technique is sometimes applied to maintain permafrost conditions in northern regions, notably for roads [1].

The general technique for AGF has remained mostly identical to what it was in the early days. Figure 1.2(i) shows a typical AGF freeze pipe. Installation typically proceeds as follows:

- Hole drilled using regular techniques
- Metal casing incrementally added to help maintain hole wall integrity
- Grout added at the end to "cap it off"
- Inner pipe inserted
- Header installed and freeze tube connected to coolant network

Casing and inner pipe usually have a length of around 10m and are interconnected using a screwing interface. The outer casing is always metallic, while the inner pipe is sometimes made of PVC.

The number of variables in AGF process makes it difficult to make systematic studies based solely on field data. To solve this issue, a number of experimental and numerical models have been created. These will be explored in the following sections.

2.3.1 Experimental Studies

Ständer performed one of the first systematic experiment on AGF. In this study, 5 single straight 5mm diameter tubes were installed in sand with a spacing of 70mm. The ground temperature was initialized by flowing water through the sand-filled box. Once the sand had reached equilibrium, the freezing process debuted. Victor [23] used the same setup and added vertical flow.

Table 2.1: Summary of Freezing Experiments (Adapted from [28])

Model	Size [cm]	r_o [mm]	Spacing [mm]	T_{soil} [°C]	T_{pipe} [°C]	Duration [h]
[29]	100 X 30 X 90	2	Single pipe	10	-30	2
			42 (circular)	14.7	-16	4
				20	-23.4	
[23]		2.5	70	25	-23.7	3 to 12
				5	-15.5	
[24]	50 X 50 X 130	19	450	8	-25	30
[28]	120 X 130 X 100	20.5	322	15 to 21	-23 to -15	12 to 76
[26]	100 X 100 X 100	60.3	single	20	-183	32

Berggren performed a similar experiment in 1982 ([24]), but with some modifications. They installed three parallel bayonet freeze tubes and controlled horizontal groundwater flow using difference in water head. Only low flow rates were achievable with this setup.

In 2007, Pimentel [25] built a model to study the effect of high velocity groundwater flow on AGF. A similar setup of three aligned vertical bayonet tubes in a horizontal box filled with sand was devised. The results were then used to validate a numerical model.

Other experiments have used cylindrical sand domains to take advantage of axisymmetric conditions for numerical modeling. This is the case for Gioda et al [26]. This experiment consists of a single bayonet freeze tube within a cylindrical enclosure. Liquid nitrogen is the cooling fluid; the system can operate between -182°C and -80°C. The results were used to validate a numerical model. Temperature is recorded at the tube's mid-height within the sand.

To assist the study of AGF, Fabbri devised an apparatus that can measure the ice concentration using ultrasonic and dielectric measurements [27]. This could increase the accuracy of future experimental setups.

Table 2.1 contains a summary of the different experiments and their properties. It has been adapted from [28].

2.3.2 Mathematical Models

All of the models presented in Section 2.2.2 can model ground freezing with varying degrees of accuracy. However, only a few have been applied to the artificial ground freezing problem. Often, commercial software will be sufficient for the level of accuracy required on field. For instance, [30] successfully uses

Table 2.2: Annular Flow Regimes

Regime	H=1	H>5, Pr=1
Conduction	$Ra/H \leq 1000$	$Ra/H \leq 400$
Transition	$1000 < Ra/H \leq 8000$	$400 < Ra/H \leq 3000$
Boundary Layer	$Ra/H \geq 8000$	$Ra/H \geq 3000$

the commercial software TEMP/W to model AGF in mining applications while [31] uses COMSOL. Vitel [32] also created a coupled numerical model of a single freeze pipe, which has the advantage of being computationally faster but less versatile.

2.4 Natural Convection in Annulus

Natural convection in closed annulus has been studied extensively both experimentally and numerically: experimental studies strive to find correlations for the Nusselt number while numerical studies are usually more interested in validating a framework and analyzing the isotherm and velocity profiles. Research has then been dealing with mostly the same problem formulation but with some topical differences: boundary conditions, Prandtl number, Rayleigh number and geometry.

The general form of the correlation (Equation 2.1) is exponential and has been applied since at least 1969 [33].

$$Nu = C_1 Ra^{c_2} H^{c_3} \kappa^{c_4} \tag{2.1}$$

Where C_1 is a function of Pr, $H = L/(r_o - r_i)$, $\kappa = r_o/r_i$. Correlations can use either $Ra = \frac{g\beta d^3 \delta T}{\nu^2} Pr$ or $Ra^* = \frac{g\beta d^4 q_c}{k\nu^2} Pr$ depending on the boundary conditions; setups with constant heat flux tend to prefer Ra^* while fixed temperature boundary conditions use Ra. The correlations found in literature depend greatly on which flow regime is present, and by extension, on the Rayleigh number (Table 2.2). A summary of available correlations based on experimental and numerical findings is provided in Table 2.3.

It is worth noting that $\kappa \approx 1$ approximates to parallel plates while $\kappa \geq 5$ tends to cylindrical solutions.Therefore, authors may use D_H as specific length [39]. The aspect ratios usually are much greater than unity; an infinite

Table 2.3: Heat Transfer Correlations for Natural Convection in Annulus

Experimental											
Reference	BC	Range of Ra		H	κ	Pr	c1	c2	c3	c4	extra
[34]	HF - FT	$1*10^3$	$6.6*10^3$	27.60	4.32	0.71	1.406	0.077	-	-	-
		$6.6*10^3$	$2.3*10^6$				0.163	0.322	-	-	-
							0.595	0.101	-0.052	0.505	$Pr^{0.024}$
[35]				1 - 33	1 - 10	0.5-1E4	0.202	0.254	-0.025	0.423	$Pr^{0.97}$
							0.286	0.258	-0.238	0.442	$Pr^{0.006}$
[36]	FT - FT	$1*10^4$	$1*10^6$	64	1.6	20-110	-	-	-	-	-
		$7*10^7$	$1.1*10^9$				0.304	0.27	-	-	-
[37]	HF - ATM	$7*10^7$	$1.1*10^9$	24 - 67	2.03 - 3.92	0.73	0.2789	0.32	-0.385	0.534	-
		$1*10^5$	$4*10^6$				0.0832	0.032	-	-	-
[38]	HF - FT	$4*10^5$	$4*10^6$	52 - 55	5 - 10	0.7	433.45	0.187	-0.187	-0.09	-
[39]	HF - ATM			55.2	6.25	0.7	0.253	0.244			
[40]	HF - FT			38 - 228	1.03 - 1.23		0.25	0.3	-0.25	-	-
Numerical											
[33]	FT - FT	$1*10^4$	$1*10^5$	1 - 20	1 - 4	0.5 - 5	f(Pr,κ)	0.3	-0.333	-	-
[41]	HT - FT	$1*10^3$	$7*10^4$	$\gg 1$	1 - 5	0 - 100	-	-	-	-	-
[42]	HT - FT	$1*10^5$	$7*10^5$	∞	1-∞	0.71 - 3.5					
[43]	FT - FT	$4*10^2$		>10	>5		0.455	0.202	-	-	-
[44]	FT - FT	$1*10^4$	$1*10^7$	1 - 100	0.5	0.73 - 25					
[45]	HF - FT			13.80	4.32	0.71	0.281	0.322	-0.407	0.555	-

BC= Boundary conditions, HF= Constant Heat Flux, FT=Constant Fixed Temperature, ATM=To Ambient Atmosphere.

ratio tends to solutions of open annuli when fixed temperature boundary conditions are used [42]. Smaller aspect ratios have been more prominent in qualitative or visual investigations [44]. The most common Pr studied are ≈ 0.7, 3.5, 100 and 0 for air, water, oil and vacuum respectively. Finally, the global range of Ra studied generally vary from $1*10^3$ to $1.1*10^9$.

Chapter 3

Experimental Setup

3.1 Introduction

Artificial ground freezing concepts and its applications were discussed in Chapter 2. As mentioned, no experiments have been done with insulated freezing tubes before. Therefore, while we do have indications of how well these tubes work in-situ [28], conditions on the field are too variable to pinpoint with accuracy the exact conditions. Another advantage of controlled experiments is the certainty that geometries such as alignment are respected. As will be seen in Chapter 5, this can greatly impact the performance of freezing tubes. Finally, since AGF project durations range between months and years [20], experiments will allow data collection within a reasonable time.

3.2 Physical Setup

3.2.1 Overview

Figures 3.1 and 3.2 show the flowsheet and laboratory setup respectively with the main components. The chiller provides the cold coolant. It has an internal pump but the IBFT's pressure drop requires the additional pump. A Proportional Relief Valve controls a bypass loop to ensures pressure does not exceed the flowmeter's maximum. Flow can be directed to the IBFT using a three-way valve. A metering valve and a variable frequency drive (VFD) control the flow rate to a steady value. The IBFT itself is set inside a tank filled with saturated sand. The tank is surorunded by heating bands to assist

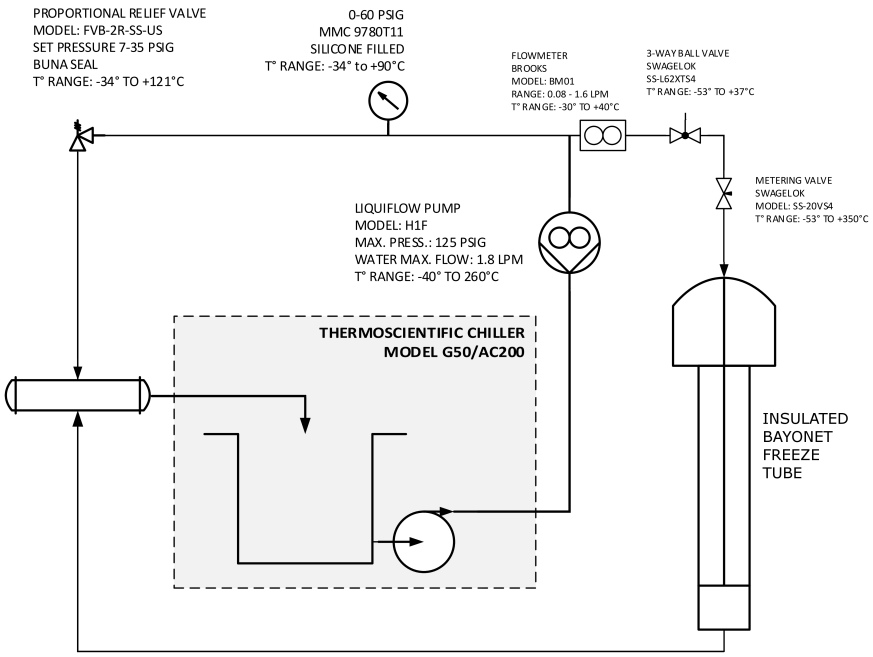

Figure 3.1: Flowsheet of Insulated Bayonet Freeze Tube Setup

preconditioning of the sand, and by multiple layers of thermal insulation.

Two types of data are recorded: temperature and flow rates. For temperatures, thermocouples are installed around the IBFT on three different levels within the sand. Thermocouples are also installed at the inlet and outlet of every freezing tube to monitor the coolant's temperature. A digital flowmeter monitors the flow at the inlet and serves as feedback for the VFD's PID control.

3.2.2 Tank and Sand

The cylindrical aluminum tank is 1638 mm tall and has a diameter of 549.3 mm. It was manufactured by soldering a 9.525 mm base onto a cylinder made of a bent 6.35 mm thick aluminum sheet. A soldered flange at the top is screwed to a metal support holding the pipes. A 1/8" thick rigid rubber mat rests under the tank while two 1/2" Styrofoam plates lay on the inside. A closed cell moisture resistant layer surrounds the tank, followed by

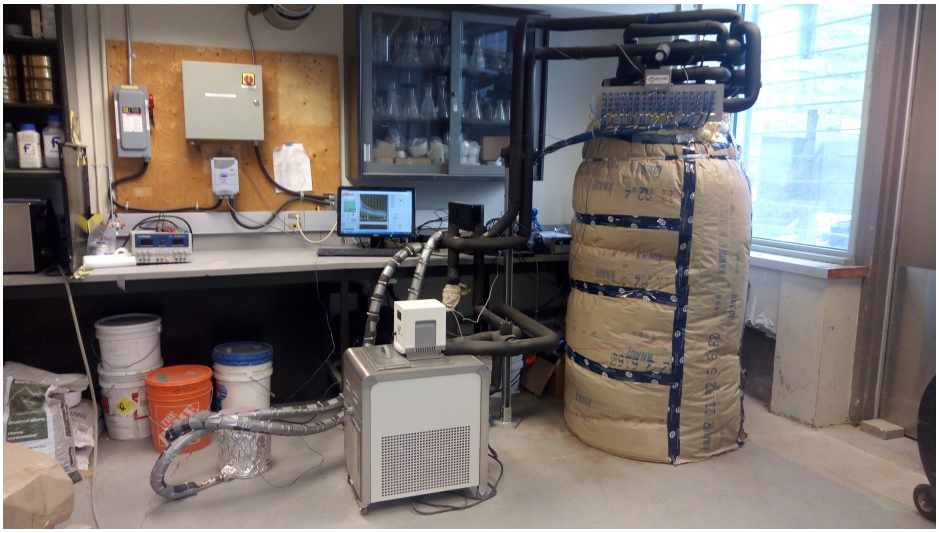

Figure 3.2: Whole experiment in lab setting

1" of foam membrane and two layers of 3-1/4" thick fiberglass insulation. Insulating spray foam was used to seal the top of the tank and complete the insulation.

The tank is filled with regular construction sand and tap water to a porosity of 37%. The sand was riffled and deposited in 90 kg batches. After each batch, 20 L of water was added to reach saturation. After 24 hours of resting period, the excess water over-saturating the sand (0.3 L) was removed. Another two plates of Styrofoam cap the top of the sand. During the course of he experimental runs, the sand has been re-saturated to compensate for the loss of water due to natural evaporation. The detailed properties of the sand can be found in Section 3.4 below.

3.2.3 Insulated Bayonet Freezing Tube and Piping

The IBFT assembly consists of a 1-1/4" outer pipe, a 1/2" inner pipe and a 1" pipe to make the insulation. All these pipes are made of ANSI316 stainless steel to ensure alignment and ease of assembly. The outer pipe is capped-off at the bottom and penetrates the sand for a depth of 1532mm. 1" separates the end of the inner pipe from the outer end cap. The insulating pipe has a length of 762 mm; a soldered metal ring connects the outer and insulating pipe. Teflon spacers glued on this final pipe ensure the whole assembly is

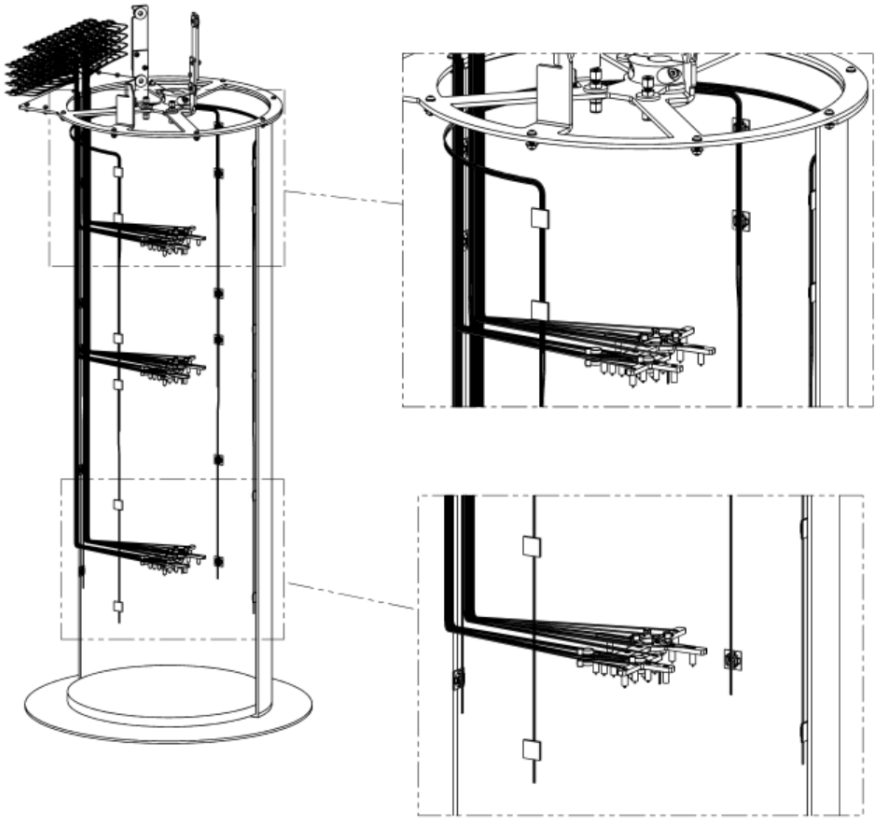

Figure 3.3: Cross-section showing instrumentation

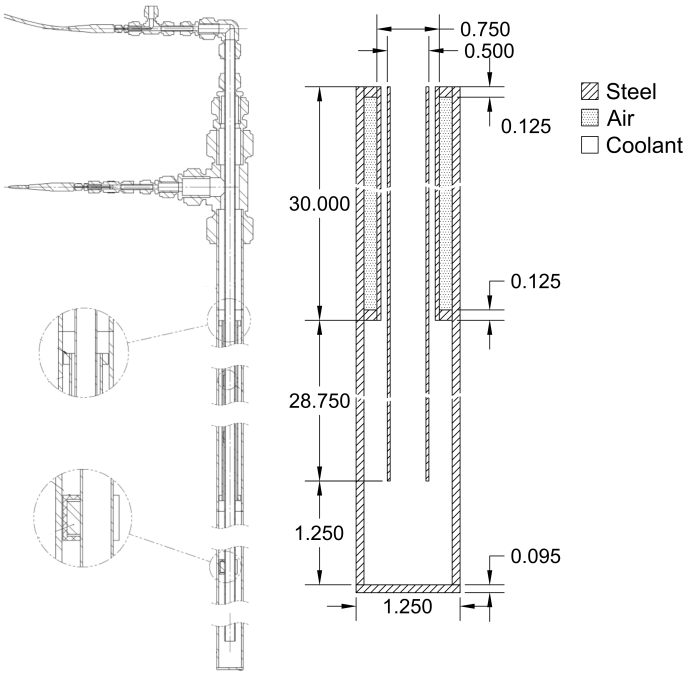

Figure 3.4: Insulated bayonet freeze tube assembly (dimensions in inches)

concentric. Figure 3.4 gives an overview of the main details with dimensions.

The IBFT rests on the metal support mentioned in Section 3.2.2. A 1/2" thick Teflon ring between the pipe and support prevents direct metal to metal conduction. The Teflon ring also ensures the IBFT stays vertical during assembly. Furthermore, horizontal acrylic centering spacers are installed at the middle and below the pipe to provide steady and accurate spacing to the wall (See Figure 3.3)

3.2.4 Coolant, Chiller and Pump

Field applications of AGF often use Calcium Chloride ($CaCl_2$) [19]. However, to prevent possible corrosion in the system and to ensure compatibility with the chiller, Ethylene Glycol ($(CH_2OH)_2$) diluted to 55% by volume was selected instead.

A Thermo Scientific G50 GLACIER refrigerated bath circulator maintains the coolant's temperature. This instrument can cool or heat glycol

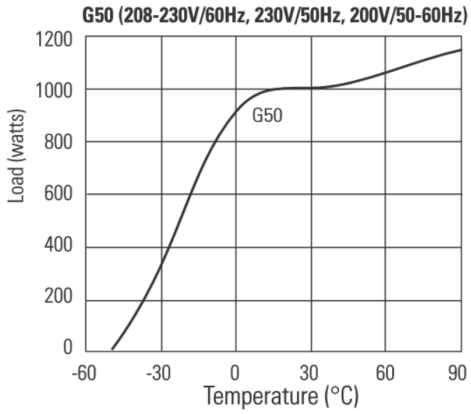

Figure 3.5: Nominal cooling capacity of the G50 Chiller (from [46])

from -30° C to 70° C with an accuracy of 0.01° C. However, it is less efficient at low temperatures and can only provide between 400 W at -30° C compared to 1000 W at room temperature as can be seen in Figure 3.5.

While the G50 has an internal pump its power is not sufficient to provide flow to all of the experiments as required. A 1/4 HP Liquiflo H1X gear pump is installed after the chiller providing up to 32 ml/s and 15.5 bar. This pump is connected to a VFD (see Section 3.3.3) to ensure steady flow. Needle valves are located on the piping network to further regulate the flow if required.

3.2.5 Piping

Around 3.1 m of 3/8" pipes is required to connect the pump to a manifold on top of the tank, while 3.2 m of similar pipes return the coolant to the chiller. A three-way valve after the pump allows auxiliary systems to use the chiller and pump. The manifold is made of 1/4" pipe and can redirect the coolant to any of the 5 freeze pipes as required. This section is supported by aluminum brackets to ensure stability. 9 mm thick Teflon rings inserted between pipes and brackets reduce metal to metal conduction. A FLUFLO FV Proportional Relief Valve set for 35 PSI is installed in this section to prevent instrument damage. Three layers of 1" thick Armaflex insulation are installed around every pipe and valve, on the pump head and on some of the support brackets.

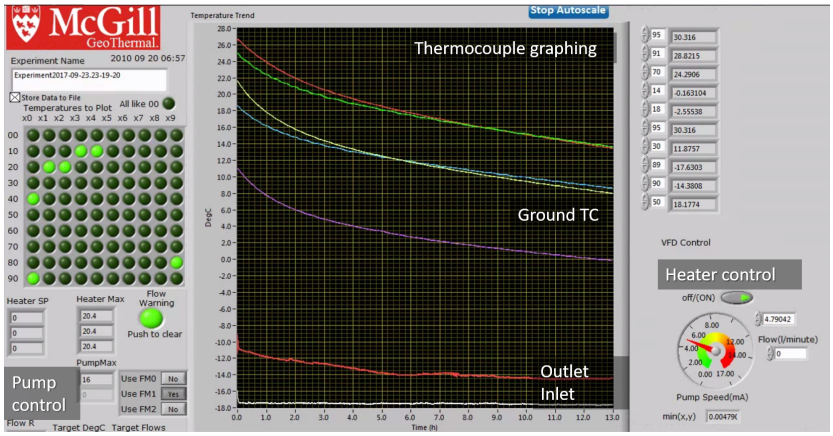

Figure 3.6: LabVIEW Environment for the experiment

3.3 Measurement and control

3.3.1 Data Acquisition Instruments

Data acquisition is taken care of using three main instruments: a National Instruments compact Data Acquisition system (cDAQ), an Agilent Multiplexer and National Instrument compact field point (cFP). These three instruments read and write data to and from the different sensors. The cDAQ-9178 chassis has three NI9211 temperature input modules and a NI9221 voltage input module. The Agilent Multiplexer reads the temperature of 60 thermocouples, but with a lower sampling rate compared to the DAQ. The NI cFP-1808 chassis is equipped with three cFP-TC-125 modules and cFP-CB-3 combos that can read up to 8 thermocouples each. A cFP-PWM-520 and a cFP-AO-200 module are installed to send signals to other instruments. The cDAQ, the Agilent multiplexer and the cFP are all connected to a computer running a custom LabVIEW virtual instrument (see Figure 3.6). This provides the logic to control, read, and record the temperatures and flow rates, and can send emails warnings when any of these differ from the setpoints. Data recording is set at every 30 seconds providing a balance between accuracy and file size.

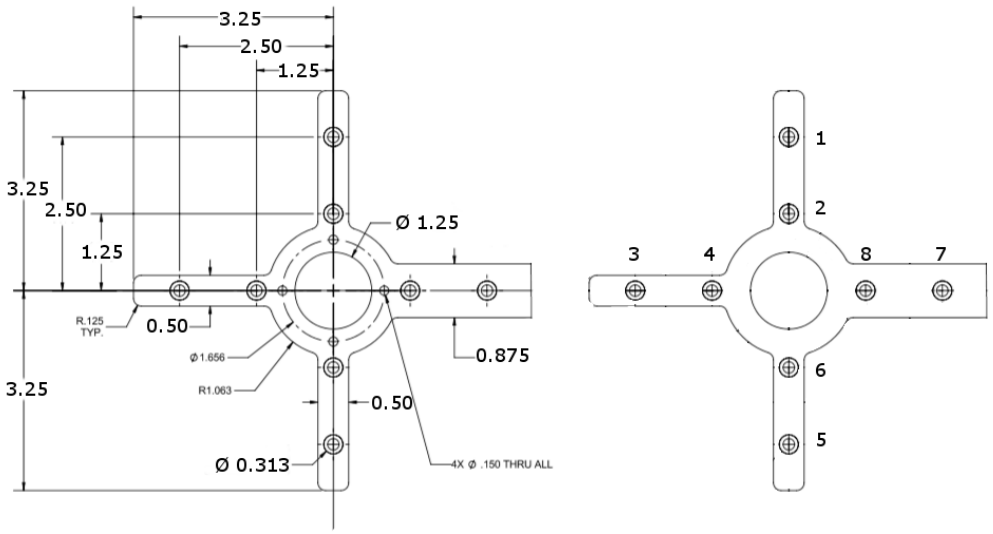

Figure 3.7: Location of the Thermocouples on the Support and TC Naming Convention (Dimensions in inches)

3.3.2 Temperature

Two fine tip TJ transition joint K-type thermocouples (TC) from OMEGA are installed at the inlet and outlet of the bayonet freeze tubes such that the tip of the TC is at the center of the flow. This reading's importance is paramount and the TC were therefore plugged into the cDAQ, which is the most reliable and least noisy instrument. The sand TC on the other hand are TC-PVC-T-24-180 T-Type thermocouples. They are epoxy tipped and therefore do not deteriorate in the sand-water environment. Teflon supports were manufactured to ensure accurate TC spacing. These have a 1" extrusion to offset the thermocouple and reduce the thermal influence of the support on the readings (See Figure 3.7 and 3.8). Three such supports are installed around the IBFT: at 304.8 mm , 660.4 mm and 1181.1 mm from the top of the sand, corresponding to active, transition and passive zone. Each Teflon support holds eight TC held in position with zip-ties to prevent movement during sand filling.

Three band heaters surround the tank to help reheat the rig after experiment runs. These have built-in J-Type thermocouples connected to the cFP. Twelve TC are installed on the inside of the tank's wall on three levels: at 250 mm, 777 mm and 1304 mm from the top of the sand, which coincides

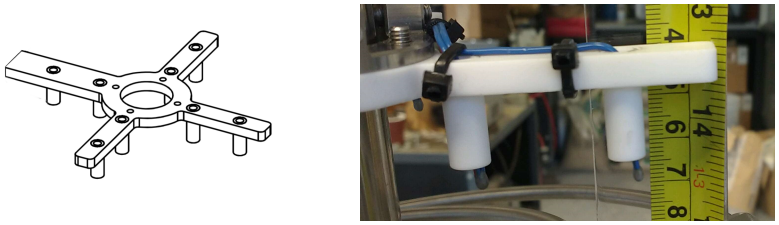

Figure 3.8: 3D model and picture of Support

with the middle of the three heating bands. These T-type thermocouples are fixed on the tank wall by an adhesive structure. For each heating band, the corresponding four TC's average temperature reading serves as the Process Variable for the PID controller. The desired wall temperature (PID Setpoint) can be set individually for each band. LabVIEW controls each band's power output as a Control Variable separately using the cFP-PWM-520 Power Modulator module

All thermocouples were calibrated prior to usage, ensuring comparable results and accurate readings. The TC were inserted in batch of 12 in a block of stainless steel which was in turn submerged in the chiller bath (Figure 3.9). For every 5°C interval between -30°C and 60°C, temperature was held steady for 30 minutes while thermocouple readings were recorded. The average of the readings was assumed to be correct, and the deviation between each thermocouple and the mean was curve-fitted into a linear correction curve. The final corrections account for less than 0.2°C and 1.5% of the temperature. A sample calibration curve for one of the wall thermocouples is provided in Figure 3.10

3.3.3 Flow Rate

A Brooks BM-01 oval flow meter records the volumetric flow in the freeze tube inlet. It operates by using slight pressure differentials to rotate two internal oval gear. A sensor detects each rotation thanks to a magnet built into one of these oval gears which creates a voltage differential detected by the NI9221 module on the cDAQ. The connection diagram can be seen in Figure 3.11. The flowmeter has a nominal calibration of 1 pulse per ml, is rated to -30°C and has a rated accuracy of 1% with a maximum working pressure of 75 PSI. The LabVIEW program transforms the volume reading into flow-rate. During experiments, the flow is regulated via a PID control in

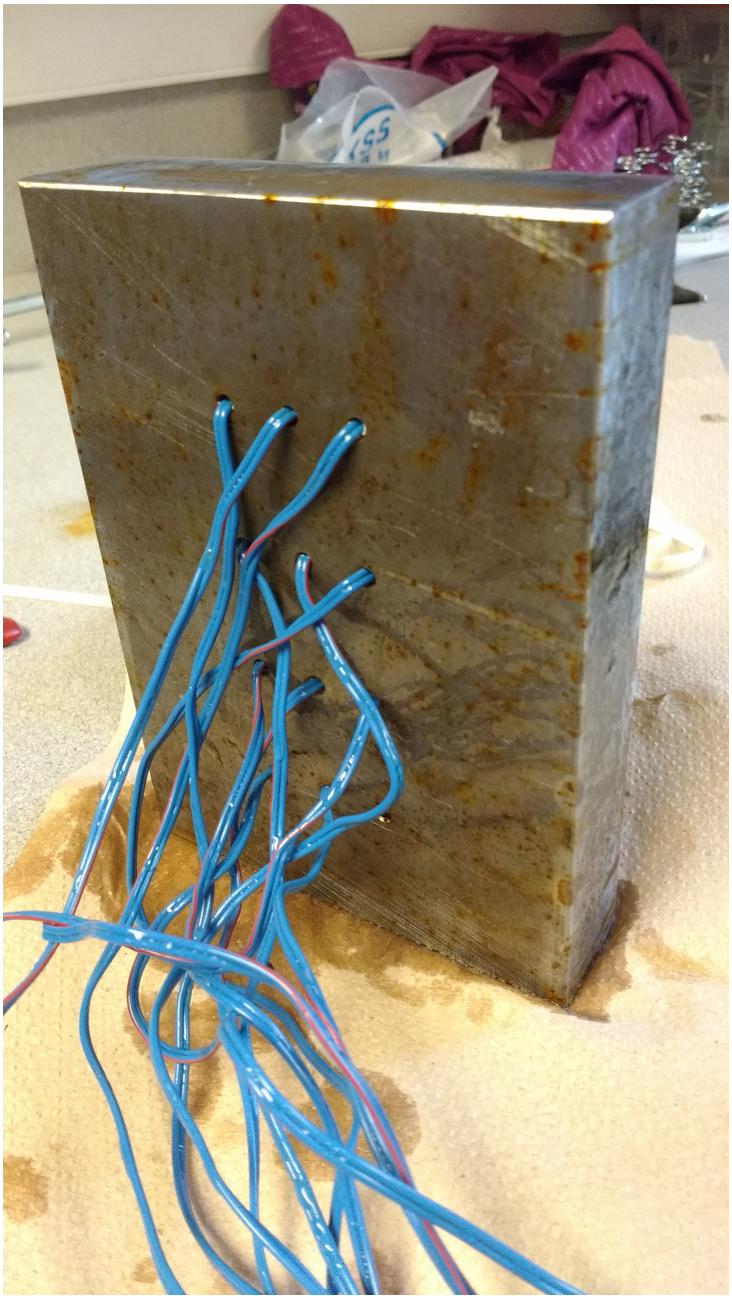

Figure 3.9: Calibration Setup for Thermocouples

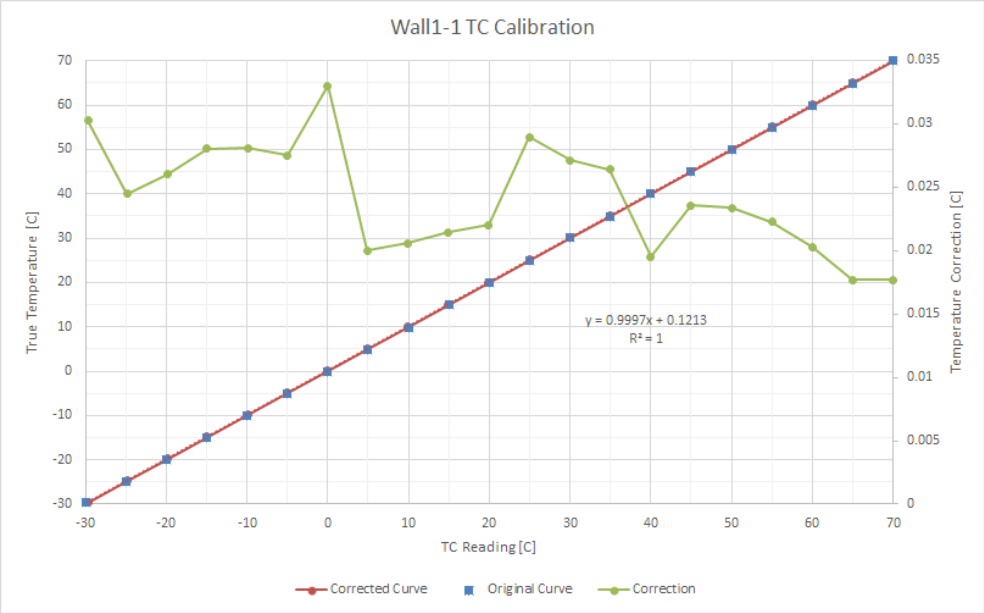

Figure 3.10: Sample Thermocouple Calibration Curve

LabVIEW. A WEG CFW08 VFD controls the rotation speed of the pump based on the 0-20 mA feedback from the cFP. This procedure can achieve a consistent flow rate with a variance of less than 0.1 ml/s.

3.3.4 Pressure

An analog pressure gauge is installed in the pipe to monitor the pressure and prevent leaks due to overpressure. The Proportional Relief Valve mentioned in Section 3.2.5 was adjusted using this instrument.

3.4 Material Properties

3.4.1 Measurement

The property for Glycol and Sand were measured in the Lab and are summarized in Table 3.1. For Ethylene Glycol, property curves at different concentrations are well documented and available, for example from manufacturers. Thus, the main concern for Ethylene glycol was to determine experimen-

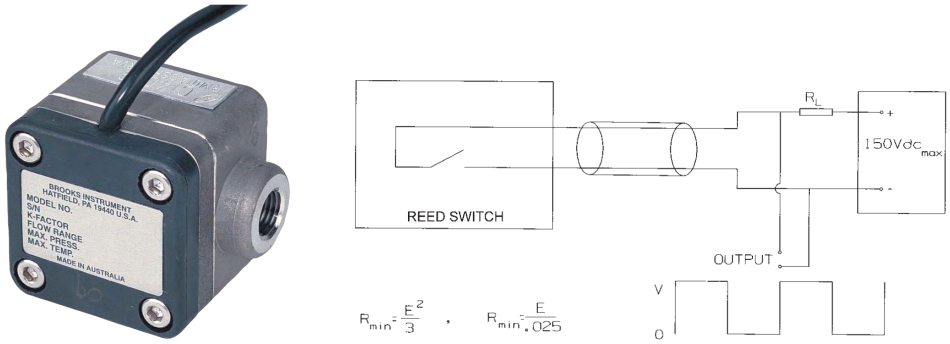

Figure 3.11: Flowmeter and Connection Diagram (from [47])

tally the concentration from which temperature dependent property curves can be used. On the other hand, sand properties are not standard. The measurements were thus used to create the curves.

The main properties tested include density, thermal conductivity and specific heat. Viscosity and porosity were also measured when applicable. These properties were taken at different temperatures between -30° C and 30° C to have a representative curve of the properties on the whole experimental range. Temperature control was achieved using the auxiliary circuit mentioned in Section 3.2.5.

Glycol

Initial concentration was calculated based on the volume of water and glycol mixed using a 2L graduated cylinder. However, this proportion changes slightly over time due to evaporation. Density, viscosity and thermal conductivity were therefore measured and compared to the available curves. Density was measured using a titration column and a digital scale accurate to 10 mg. The higher variance at lower temperature is in part due to the heat gain of the liquid during manipulation. Viscosity was recorded using a Thermo Scientific viscometer. The bulbs available were only rated from 0.015 PaS to 1.5 PaS and therefore measurements above 0°C cannot be considered accurate, and explains the discrepancy in Figure 3.12. KD2-Pro thermal properties analyzer was used to measure the thermal conductivity. This device is ASTM D5334 compliant and functions by pulsing energy through a needle and measuring its response. The specific heat of sand and glycol was measured using a small-scale calorimeter consisting of a heating element and a thermocouple.

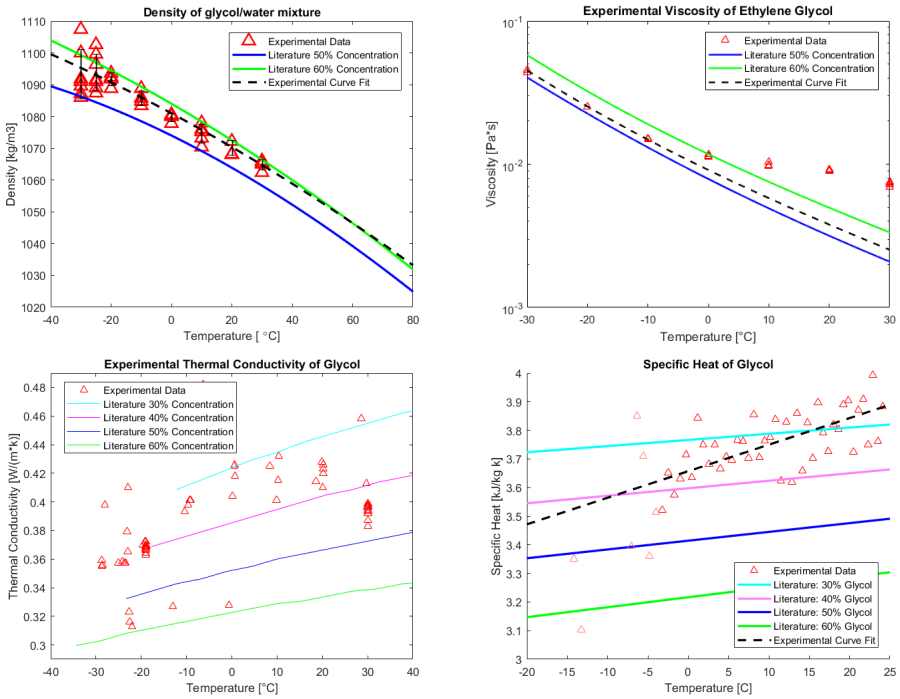

Figure 3.12: Measured Glycol Properties

The effect of ambient heat gain was factored in the calculations.

Sand

For the sand, the chemical composition was determined using X-Ray Diffraction (XRD). The grain density was assumed based on this composition of 90.5% quartz and 9.5% albite (Figure 3.13). The thermal conductivity was measured using the KD2-Pro probe, which records bulk conductivity. Measurements were done in both dry and saturated conditions at different temperatures to isolate the sand particle properties. As discussed in Chapter 2.2.1, geometric mean was used to isolate for the grain value. The porosity was measured by taking a representative test sample of the sand and pouring it into a beaker. Water was then added until saturation. The mass of water and sand was recorded and the porosity was calculated to 37%. For the sand in the tank itself, the same procedure was used: the weight of sand used was recorded alongside the volume of water used to calculate the porosity. A

Table 3.1: Experimental Thermo-Physical Properties of Glycol and Sand

Property		Glycol (-20°C)	Error
Composition		55% Ethylene Glycol 45% Water	± 2%
Density	[kg/m^3]	1090	± 0.42
Thermal Conductivity	[w/mK]	0.34	± 5%
Specific Heat	[J/kgK]	2900	± 5%
Viscosity	[PaS]	0.0253	5%
Property		**Sand (25°C)**	**Error**
Composition		90.5% Quartz 9.5% Albite	± 1.5%
Density	[kg/m^3]	2650	-
Thermal Conductivity	[w/mK]	3.72	± 5%
Specific Heat	[J/kgK]	946	-
Porosity	[-]	0.37	± 0.02

similar value of 37% was obtained. Water is added periodically to the tank to ensure saturation is maintained.

3.5 Repeatability of Results

To ensure the validity of the results, we performed the experiment with the same operating parameters three times within a week. The sand's initial temperature was set to 20 °C, glycol flowrate was set to 15 ml/s and the chiller setpoint temperature was set to -30 °C.

The flowrate PID exhibits shows great precision, reaching the desired setpoint within 70 seconds and maintaining it within ± 0.05 ml/s for all three trials. The variation in the inlet temperature is due to the chiller's available chilling power, as discussed in Section 3.2.4. The difference between runs is up to 1.5°C. However, the effect of this variation on the heat gain is minimal, with the deviation of heat gain is only of around ± 0.15°C, as seen in Figure 3.14.

As mentioned in Section 3.3.2, each pair of level and distance from pipes has four thermocouples monitoring the temperature. Over the course of three trials, a trends can be observed from the results in Figures 3.15-3.17. A diagram of the thermocouple locations is available in Figure 3.7

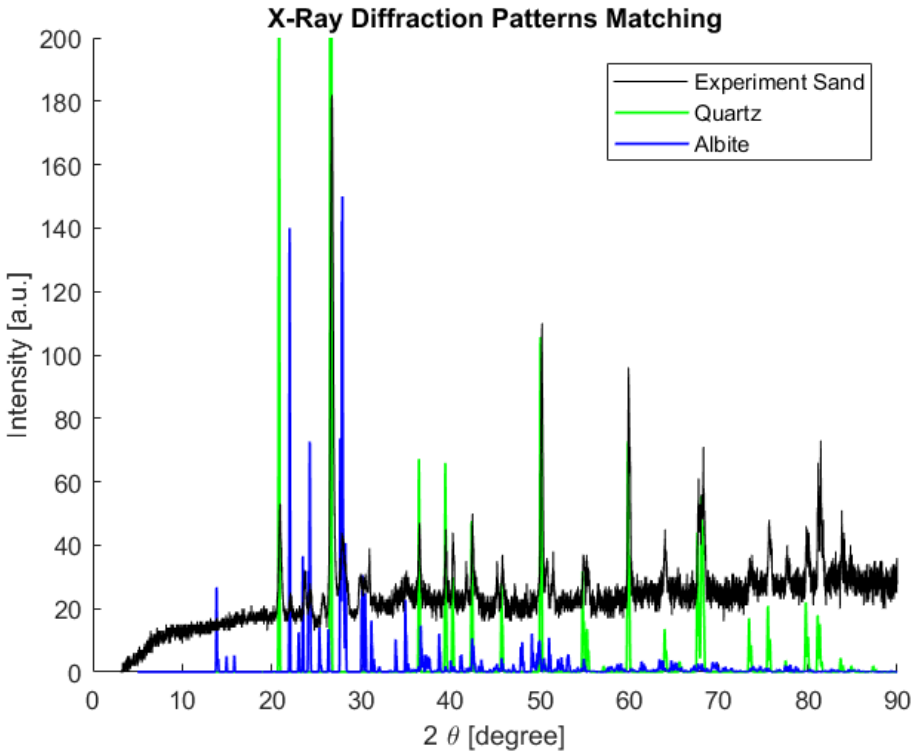

Figure 3.13: XRD Pattern Matching for Dry Sand

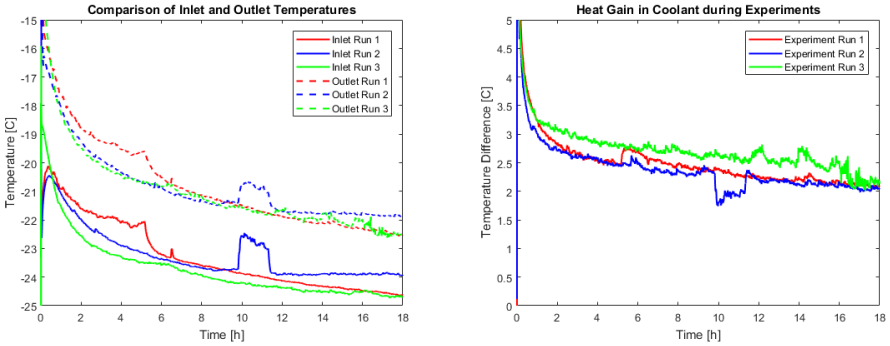

Figure 3.14: Comparison of Glycol Flow Rate and Heat Gain between experiment runs

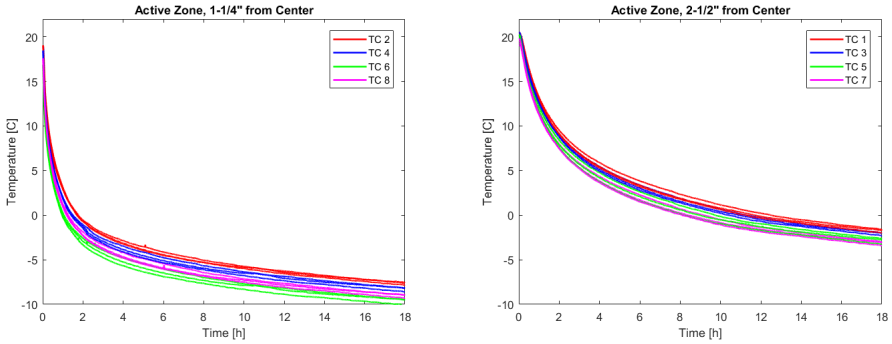

Figure 3.15: Temperature of sand thermocouples close in Active Zone

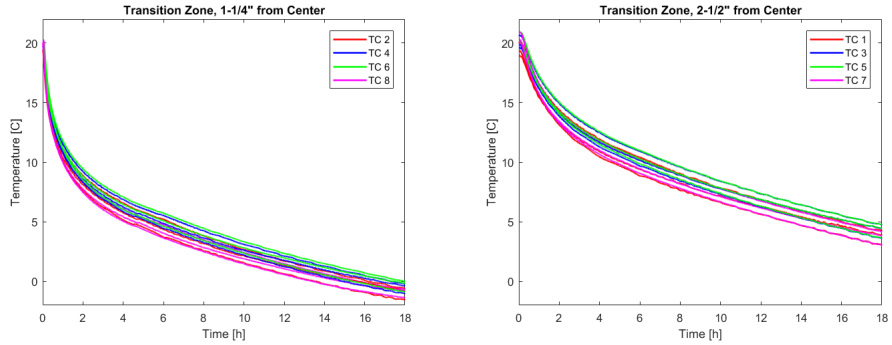

Figure 3.16: Temperature of sand thermocouples close in Transition Zone

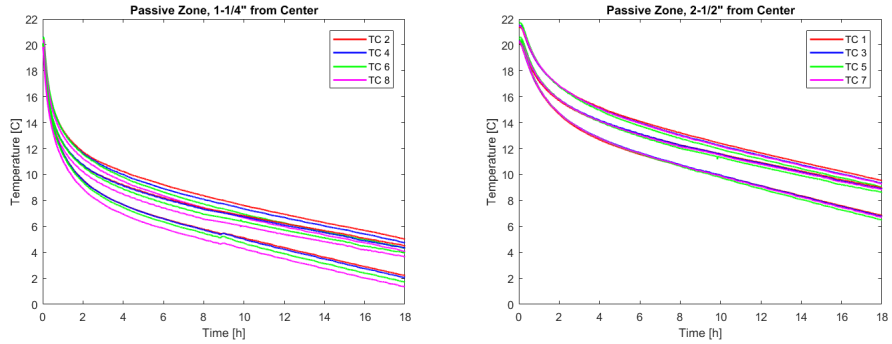

Figure 3.17: Temperature of sand thermocouples close in Passive Zone

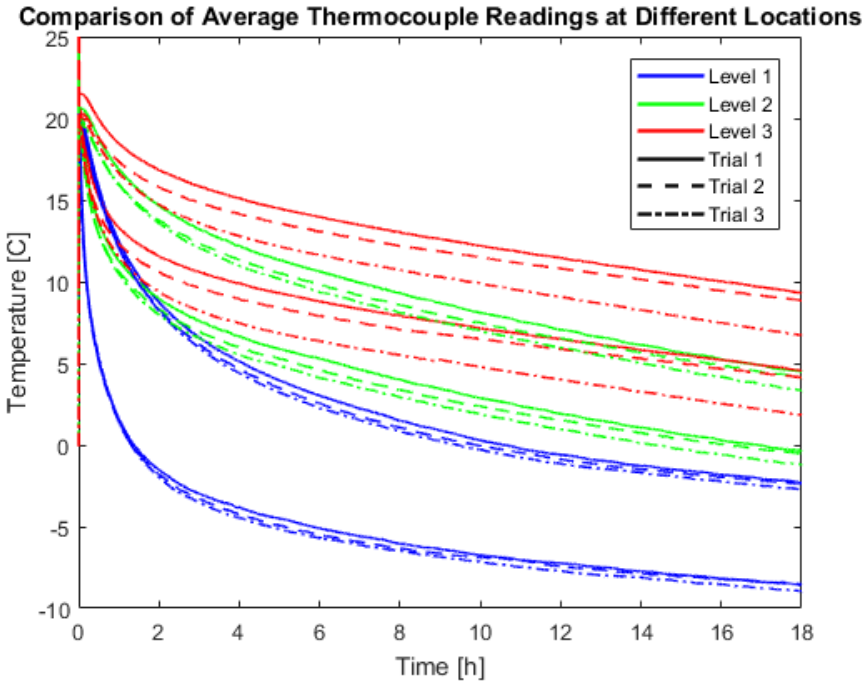

Figure 3.18: Comparison of Average Sand Temperature Readings

First, temperature distribution is not perfectly equal in all directions. There is a difference of 1.3°C at most between opposed thermocouples. This effect is most present during the first 2 hours when the temperature decreases fastest. When a thermocouple is colder than an other, it is consistently so regardless of the trial.

The average temperature readings (Figure 3.18) between trials are comparable, with negligible variations in the active and transition zone (level 1 and 2). The passive zone shows more difference which can be attributed to a change in ground saturation; the tank was resaturated after the second trial.

Finally, the initial ground temperature showed some variation between runs, most importantly in the passive zone. The ground was initialized to 20°C, but went up to 22°C due to ambient temperature. The passive zone's reduced thermal conductivity reduces our ability to fine-tune the temperature, which can cause these discrepancies.

Chapter 4

Numerical Model Development and Validation

Artificial ground freezing using insulated bayonet freeze tubes is a physical process that depends on three regions and their interactions: the coolant flow in the pipe, the natural convection in the air gap and the heat and freezing through the sand. Coolant flow and sand temperatures were validated using the experiment discussed in Chapter 3. The air insulation's validation was performed using data from [34]. We selected this dataset among the ones reviewed in Chapter 2 due to the similarity between their values for Ra and Pr compared to our scale experiment.

4.1 Natural Convection in Closed Annulus

4.1.1 Experimental Model

Keyhani's experimental setup for natural convection in closed annulus consists of a heating rod inside a cylinder capped-off at both ends. Figure 4.1 shows the main dimensions of the device. It consists of a stainless cylinder whose ends are capped by aluminum plates screwed into place. A magnesium oxide electric heating rod is screwed into the upper cap and provides an uniform heat flux while coils on the cylinder's outer surface maintain a constant temperature of 25°C. A valve allows the gas to be changed or pressurized, although the data most relevant to use is with air at 1 atm.

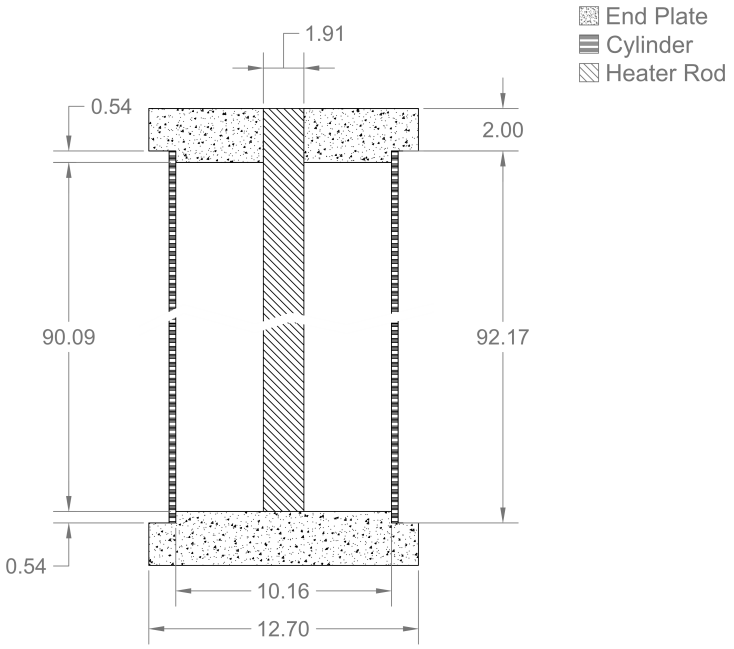

Figure 4.1: Schematics of Keyhani's experimental setup

Table 4.1: Material Properties for Natural Convection

Property	Air (20°C)	Steel	Aluminum	MgO
ρ	1.205	8030	2719	3580
k	0.0242	36	202.4	60
c_p	1005	502.48	871	1030
μ	1.846 E-5	-	-	-
ϵ	-	0.6	0.6	0.6

4.1.2 Numerical Model

Modeling

The simulation was performed using the ANSYS FLUENT commercial software. A rectangular mesh with 152,000 elements was used. To simplify the model, an axisymmetric model was used to perform the numerical simulation.

Boundary Conditions

Constant heat flux and constant temperature boundary conditions were used for the heater rod and the outer cylinder respectively. Since the end-caps are made of aluminum, they had to be modeled as their direct contact with the outer cylinder caused the to often be cooler than the heater rod. The numerical model also takes into account the contact resistance due to the screwed assembly by adding $0.001m^2/w$ on these surfaces.

Material Properties

Material properties are from literature, and air is assumed to be an ideal gas with temperature dependent thermal properties. These are summarized in Table 4.1.

Equations

In this model, mass, momentum and energy equations expressed in cylindrical coordinates govern the flow. A low Reynold number allows laminar flow conditions to dominate. This model was solved in the commercial software ANSYS FLUENT using transient calculations until a steady state was reached to account for the development of natural convection. Equations (4.1) to (4.4) describe the conservation equations.

Conservation of mass

$$\frac{\partial \rho}{\partial t} + \frac{\partial}{\partial z}(\rho u_z) + \frac{\partial}{\partial r}(\rho u_r) + \frac{\rho u_r}{r} = 0 \tag{4.1}$$

Conservation of momentum:

Axial:

$$\frac{\partial}{\partial t}(\rho u_z) + \frac{1}{r}\frac{\partial}{\partial z}(r\rho u_z u_z) + \frac{1}{r}\frac{\partial}{\partial z}(r\rho u_r u_z)$$
$$= -\frac{\partial P}{\partial z} + \frac{1}{r}\frac{\partial}{\partial z}\left[r\mu\left(2\frac{\partial u_x}{\partial z} - \frac{2}{3}(\nabla\cdot\mathbf{u})\right)\right] + \frac{1}{r}\frac{\partial}{\partial r}\left[r\mu\left(\frac{\partial u_z}{\partial r} + \frac{\partial u_r}{\partial z}\right)\right] + \rho\mathbf{g} \tag{4.2}$$

Radial:

$$\frac{\partial}{\partial t}(\rho u_r) + \frac{1}{r}\frac{\partial}{\partial z}(r\rho u_z u_r) + \frac{1}{r}\frac{\partial}{\partial r}(r\rho u_r u_r) = -\frac{\partial P}{\partial r} + \frac{1}{r}\frac{\partial}{\partial z}\left[r\mu\left(\frac{\partial u_r}{\partial x} + \frac{\partial u_z}{\partial r}\right)\right]$$
$$+ \frac{1}{r}\frac{\partial}{\partial r}\left[r\mu\left(2\frac{\partial u_r}{\partial r} - \nabla\cdot\mathbf{u}\right)\right] - 2\mu\frac{u_r}{r^2} + \frac{2}{3}\frac{\mu}{r}(\nabla\cdot\mathbf{u}) \tag{4.3}$$

Conservation of energy:

$$(\rho c_p)_{eff}\left(\frac{\partial T}{\partial t} + u_r\frac{\partial T}{\partial r} + u_z\frac{\partial T}{\partial z}\right) = k\left(\frac{1}{r}\frac{\partial}{\partial r}\left(r\frac{\partial T}{\partial r}\right) + \frac{\partial^2 T}{\partial {z}^2}\right) + S_R$$
$$\rho_{air} = \frac{PM}{RT}$$
$$S_R = -(a+\sigma_s)I(r,s) + an^2\frac{\sigma T^4}{\pi} + \frac{\sigma_s}{4\pi}\int_0^{4\pi} I(r,s')d\Omega' \tag{4.4}$$

4.1.3 Results and Validation

The numerical simulation was performed with heater rod powers ranging from 5w to 120w. Each simulation ran for the equivalent of 2 hours to ensure the system reached steady conditions. The heat flux and air velocity was monitored to confirm. The temperature profile on the heater rod was then measured and compared to the one obtained by Keyhani (Figure 4.2).

The simulated profile matches closely the experimental one. There is a slight deviation around the center that can be attributed to inner vortex of different dimensions. This is easily seen in Figure 4.3, and could be tuned by adjusting the contact resistance between the cylinder, end plates and heater rod.

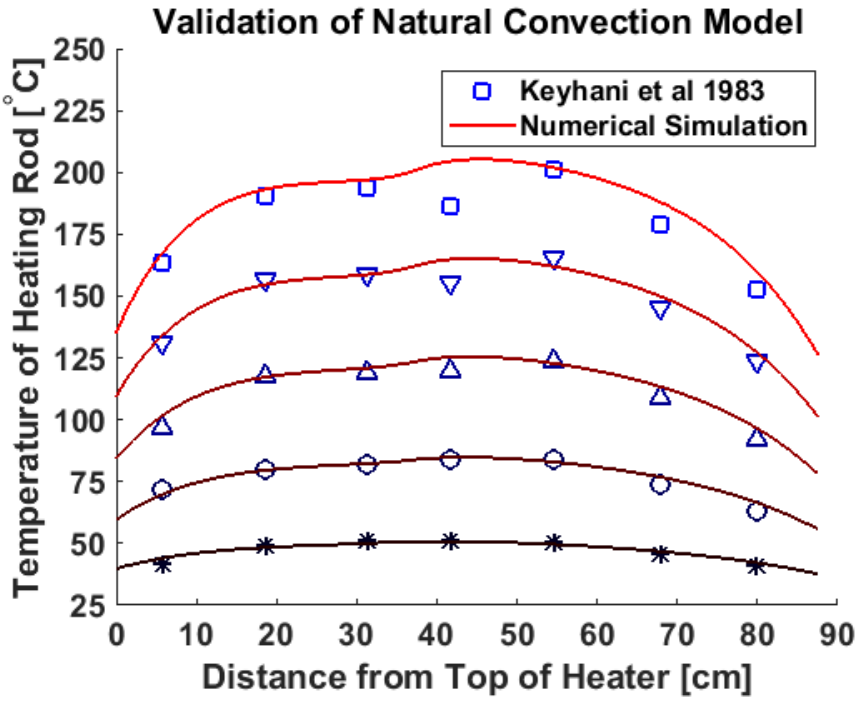

Figure 4.2: Validation of Temperature Profile on Heater Rod.
From bottom: $*$10.2W, $\circ$ 28.3W, $\triangle$ 53.99W, ∇ 83.65W, $\square$ 119.34W

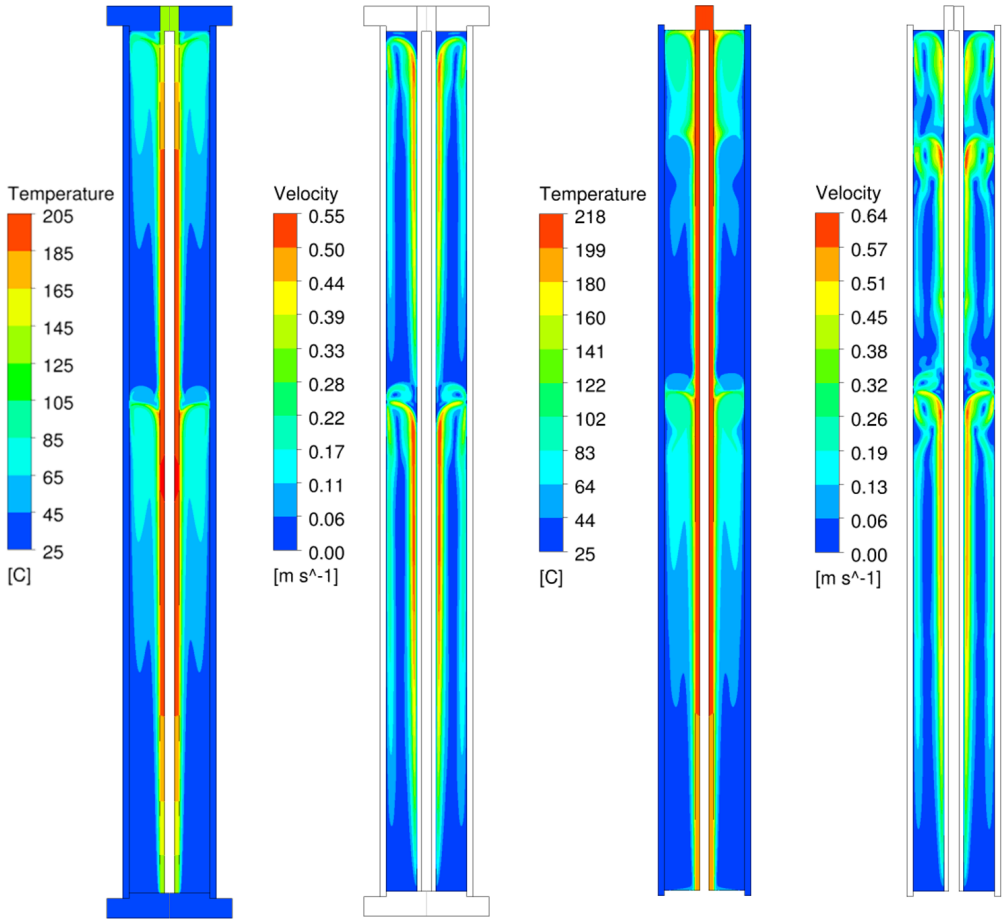

Figure 4.3: Temperature and Velocity Profile in Annular Natural Convection (119.34 W). From left: Temperature with aluminum cap; Velocity with cap; temperature without cap; velocity without cap

Again, in this case, the effect of the end cap is significant. Figure 4.3 clearly demonstrates how the temperature at the upper end of the apparatus is skewed towards the colder end of the spectrum.

It is also interesting to note the presence of two main vortices in Keyhani's experiment, which is reflected in 4.2. In this particular case, there are two smaller vortices close the top cap and between the two main ones. In comparison, when the top and bottom of the region are in adiabatic conditions, the vortices become much more important. This is also due to the higher air temperature. Further discussion of vorticity can be found in Qi ([37])

4.2 AGF in Laboratory Environment

4.2.1 Numerical Model

The natural convection model was extended to our experiment's IBFT dimensions. Coolant and sand were also added to represent the whole setup. The wall thicknesses were also modeled since they cause a significant reduction in cross-sectional flow area for the coolant annular flow in the passive zone; full dimensions can be found in Figure 3.4. Once again, an axisymmetric model was used to reduce the computation time. The mesh contains 525,000 elements and is refined through the use of size inflation close to boundaries.

Operating conditions were set to simulate experiment results. Two trials are validated: the first one has a coolant temperature of 5°C while the other runs at -20°C. This is done to first validate a model where freezing and latent heat has no influence on the results.

4.2.2 Boundary Conditions

In this model, the air region is bounded by the coolant and by the sand. Coolant flows from a constant mass flow inlet at the center of the tube and exits through a pressure outlet on the annulus. The sand is considered perfectly insulated at the top, bottom and side. It is also assumed to be homogeneously distributed and totally saturated. As mentioned previously, the wall thicknesses are modeled to take into account their influence on the flow. The spacers used to center the inner tube could not be included in the axisymmetric model. However, their influence should be negligible considering they are sparsely used and their thermal conductivity is low.

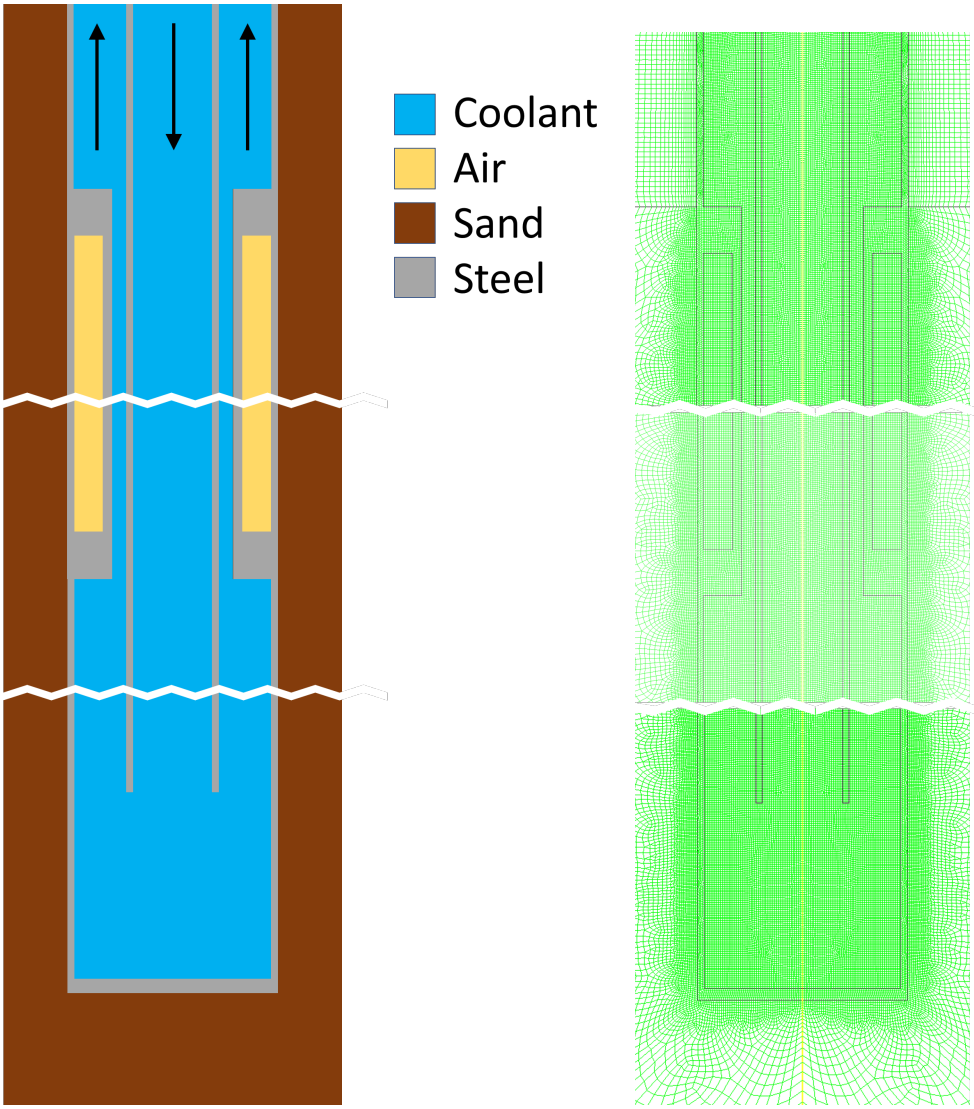

Figure 4.4: Zones and meshing of Simulation (selected regions)

4.2.3 Material Properties

Material properties used are based on the laboratory measurement and are summarized in Section 3.4.

4.2.4 Equations

Numerical modeling of the full model is more complex than when limited to natural convection, and the set of governing equations reflect this. First, the coolant region requires turbulence models due to the impingement points at the end of the pipe and at the contact with the air insulation. Secondly, the saturated sand undergoes freezing in porous medium. The air region retains the same governing equations 4.1 to 4.4 while those for the coolant and sand region are described in Equations 4.5 to 4.12.

Coolant

Conservation of mass

$$\frac{\partial \rho}{\partial t} + \frac{\partial}{\partial z}(\rho u_z) + \frac{\partial}{\partial r}(\rho u_r) + \frac{\rho u_r}{r} = 0 \tag{4.5}$$

Conservation of momentum:

Axial:

$$\begin{aligned}&\frac{\partial}{\partial t}(\rho u_z) + \frac{1}{r}\frac{\partial}{\partial z}(r\rho u_z u_z) + \frac{1}{r}\frac{\partial}{\partial z}(r\rho u_r u_z)\\ &= -\frac{\partial P}{\partial z} + \frac{1}{r}\frac{\partial}{\partial z}\left[r\mu\left(2\frac{\partial u_x}{\partial z} - \frac{2}{3}(\nabla\cdot\mathbf{u})\right)\right] + \frac{1}{r}\frac{\partial}{\partial r}\left[r\mu\left(\frac{\partial u_z}{\partial r} + \frac{\partial u_r}{\partial z}\right)\right] + \rho\mathbf{g}\end{aligned} \tag{4.6}$$

Radial:

$$\begin{aligned}\frac{\partial}{\partial t}(\rho u_r) + \frac{1}{r}\frac{\partial}{\partial z}(r\rho u_z u_r) + \frac{1}{r}\frac{\partial}{\partial r}(r\rho u_r u_r) = &-\frac{\partial P}{\partial r} + \frac{1}{r}\frac{\partial}{\partial z}\left[r\mu\left(\frac{\partial u_r}{\partial x} + \frac{\partial u_z}{\partial r}\right)\right]\\ &+ \frac{1}{r}\frac{\partial}{\partial r}\left[r\mu\left(2\frac{\partial u_r}{\partial r} - \nabla\cdot\mathbf{u}\right)\right] - 2\mu\frac{u_r}{r^2} + \frac{2}{3}\frac{\mu}{r}(\nabla\cdot\mathbf{u})\end{aligned} \tag{4.7}$$

Conservation of energy:

$$(\rho c_p)_{eff}\left(\frac{\partial T}{\partial t} + u_r\frac{\partial T}{\partial r} + u_z\frac{\partial T}{\partial z}\right) = k\left(\frac{1}{r}\frac{\partial}{\partial r}\left(r\frac{\partial T}{\partial r}\right) + \frac{\partial^2 T}{\partial {z}^2}\right) \tag{4.8}$$

Soil

Conservation of mass

$$\frac{\partial \rho}{\partial t} + \frac{\partial}{\partial z}(\rho u_z) + \frac{\partial}{\partial r}(\rho u_r) + \frac{\rho u_r}{r} = 0 \tag{4.9}$$

Conservation of momentum:

$$\begin{aligned} &Axial: \\ &\frac{\partial}{\partial t}(\rho u_z) + \frac{1}{r}\frac{\partial}{\partial z}(r\rho u_z u_z) + \frac{1}{r}\frac{\partial}{\partial z}(r\rho u_r u_z) = -\frac{\partial P}{\partial z} + \frac{1}{r}\frac{\partial}{\partial z}\left[r\mu\left(2\frac{\partial u_x}{\partial z} - \frac{2}{3}(\nabla \cdot \mathbf{u})\right)\right] \\ &\quad + \frac{1}{r}\frac{\partial}{\partial r}\left[r\mu\left(\frac{\partial u_z}{\partial r} + \frac{\partial u_r}{\partial z}\right)\right] + \rho\mathbf{g} + S_L + S_{Darcy} \end{aligned} \tag{4.10}$$

Radial:

$$\begin{aligned} &\frac{\partial}{\partial t}(\rho u_r) + \frac{1}{r}\frac{\partial}{\partial z}(r\rho u_z u_r) + \frac{1}{r}\frac{\partial}{\partial r}(r\rho u_r u_r) = -\frac{\partial P}{\partial r} + \frac{1}{r}\frac{\partial}{\partial z}\left[r\mu\left(\frac{\partial u_r}{\partial x} + \frac{\partial u_z}{\partial r}\right)\right] \\ &\quad + \frac{1}{r}\frac{\partial}{\partial r}\left[r\mu\left(2\frac{\partial u_r}{\partial r} - \nabla \cdot \mathbf{u}\right)\right] - 2\mu\frac{u_r}{r^2} + \frac{2}{3}\frac{\mu}{r}(\nabla \cdot \mathbf{u}) + S_L + S_{Darcy} \\ &S_L = uC_m\frac{(1-\gamma_w)^2}{{\gamma_w}^2} \\ &S_{Darcy} = -(\frac{\mu}{\alpha}u) \end{aligned} \tag{4.11}$$

Conservation of energy:

$$(\rho c_p)_{eff}\left(\frac{\partial T}{\partial t}+u_r\frac{\partial T}{\partial r}+u_z\frac{\partial T}{\partial z}\right)=k\left(\frac{1}{r}\frac{\partial}{\partial r}\left(r\frac{\partial T}{\partial r}\right)+\frac{\partial^2 T}{\partial_z{}^2}\right)+S_L+S_R$$
$$S_L=\phi\rho_{fluid}L\frac{\partial}{\partial t}\gamma_w+\nabla*(\rho_{fluid}u\gamma_w L)$$
$$(\rho c_p)_{eff}=\phi(\rho c_p)_{fluid}+(1-\phi)(\rho c_p)_{solid}$$
$$k_{eff}=k_{fluid}\phi*k_{solid}(1-\phi) \tag{4.12}$$

4.3 Validation against Experiment

The experimental model monitors coolant inlet and outlet temperatures, and sand temperatures in the active, passive and transition zone. These are the values that will be compared to the numerical model's results. This was done for models in the frozen and unfrozen regime to test with and without the influence of phase change. The simulation was also performed with glycol in the passive zone to see the effect of possible defects in manufacturing. Ethylene glycol's thermal conductivity is around 15 time more conductive than water. To ensure accurate representation of the data, we used the ground thermocouple redundancy to get a standard deviation of the temperature over time.

4.3.1 Air Gap Validation for IBFT

Very early, we were able to notice temperatures in the passive zone in the simulations did not match the experimental results. After further investigation, we found the heat flow in insulation for the simulations differed from the correlation predictions.

For this section, we will consider the first few minutes of the experiment when the ground is at 20°C and the coolant is at -25°C, for a $Ra = 125.3$, $\kappa = 1.4$ and $H = 194$. Conduction and radiation in annular geometries is well known and can be calculated analytically from equations 4.13 and 4.14. The empirical formula 4.15 was from [35]. The radiative heat transfer formula

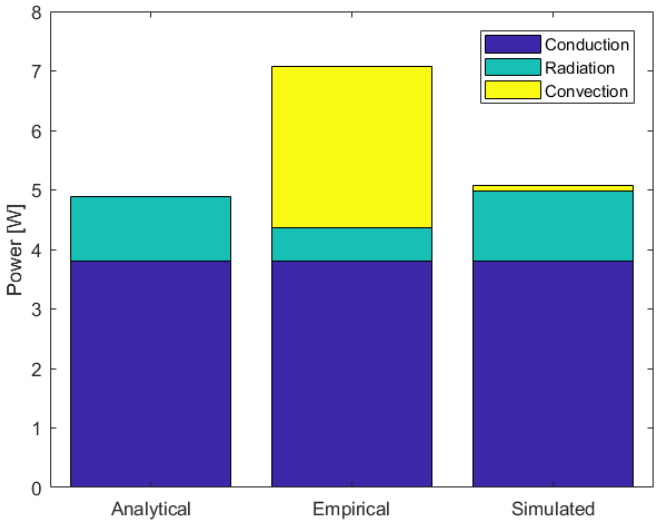

Figure 4.5: Comparison of Analytical, Empirical [35] and Numerical Results

assumes a single ϵ for all surfaces.

$$Q_{cond} = \frac{2\pi Lk}{\ln(r_o/r_i)} * \Delta T \tag{4.13}$$

$$Q_{rad} = \frac{\sigma(t_o^4 - t_i^4)}{\frac{1-\epsilon}{\epsilon 2\pi r_i L} + \frac{1}{2\pi r_i F_{12}} + \frac{1-\epsilon}{\epsilon 2\pi r_o L}} \tag{4.14}$$

$$Nu_{empirical} = 0.595 Ra^{0.101} H^{-0.052} \kappa^{0.505} Pr^{0.024} \tag{4.15}$$

When comparing the heat flow between the simulation and empirical correlations (Figure 4.5), it can be seen that the simulation has virtually no convection. On the other hand, the empirical model has a $Nu = 0.871$ which entails convection should be in the same order of magnitude. The author believes the empirical correlation is not accurate for the low aspect ratios discussed here. Some research points to the presence of instability in the flow when the air gap is this small [48], which could increase the heat transfer. To investigate this possibility, the simulation was was also run by modifying the air conductivity until experimental and simulated results matched. A Nusselt number could therefore be derived from this value.

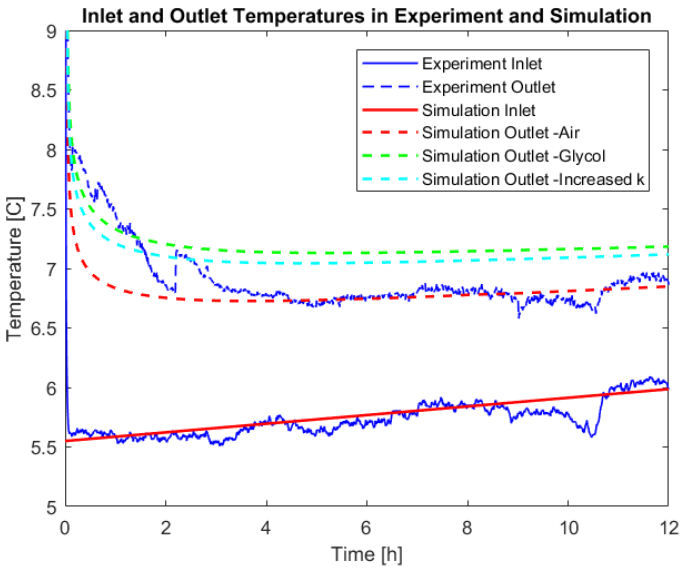

Figure 4.6: Inlet and Outlet Temperature in Unfrozen Conditions

4.3.2 Unfrozen regime

The experiment was run with a nominal inlet temperature of 5°C, a flow rate of 15 ml/s and initial ground temperature of 20°C for 15h. As mentioned, the model was run with glycol in insulation, as well as with modified air.

Coolant Temperatures

The numerical model uses a curve-fit of the recorded inlet temperature and flow rate for its boundary condition, as seen in Figure 4.6. The simulated outlet temperature fits the experimental data when air is used in the insulation. In other words, the energy balance of our model is correct.

A scenario with glycol in the insulation and with modified air conductivity increases the outlet temperature by 0.35°C and 0.28°C respectively. Both of these are within experimental accuracy, but are equivalent to a roughly 30% higher heat gain in the system

Sand Temperatures

The active, passive and transition zones are dominated by different mechanisms. In the active zone, the sand's thermal conductivity is the limiting

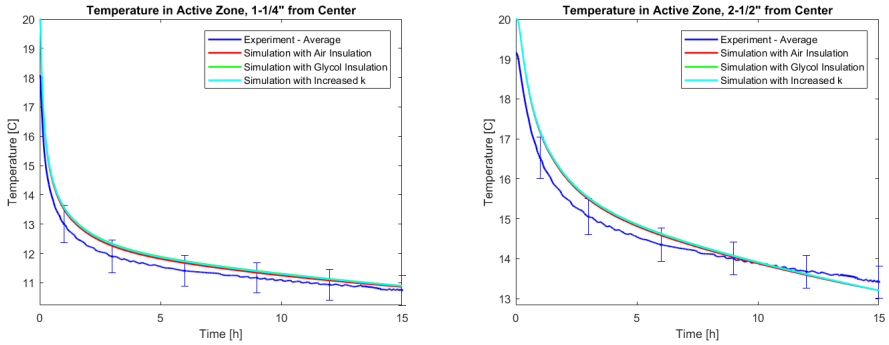

Figure 4.7: Unfrozen Sand Temperatures in Active Zone

factor to the cooling, while the passive zone depends strongly on the insulation. Finally, the transition zone is one of the few areas where the axial heat transfer is important; compared to the passive zone, the active zone's heat transfer will have a higher impact on the temperature readings.

Figure 4.7 shows a good fit between numerical and experimental values in the active zone. Unsurprisingly, the insulation's thermal conductivity bears almost no influence on the results.

The transition zone in Figure 4.8 starts to see divergence between simulations: when glycol is present in the insulation, the model over-predicts the cooling due to the increased heat transfer in the passive zone while the air insulation correctly predicts the temperature.

The passive zone underpredicts the cooling when using air in the insulation, but slightly overpredicts it when glycol is present. A Nusselt number of 9.3 (equivalent air thermal conductivity of 0.25 [W/m K]) allows a good fit with the data on all three levels. However, none of the models presented in Table 2.3 warrant such a value.

4.3.3 Frozen regime

The frozen regime adds the numerical complexity of phase change in the porous medium. Latent heat is incorporated through a enthalpy-porosity formulation. The experimental data is from the trials described in Chapter 3.5, with a nominal inlet temperature of -25°C, a flow rate of 15 ml/s and initial ground temperature of 20°C.

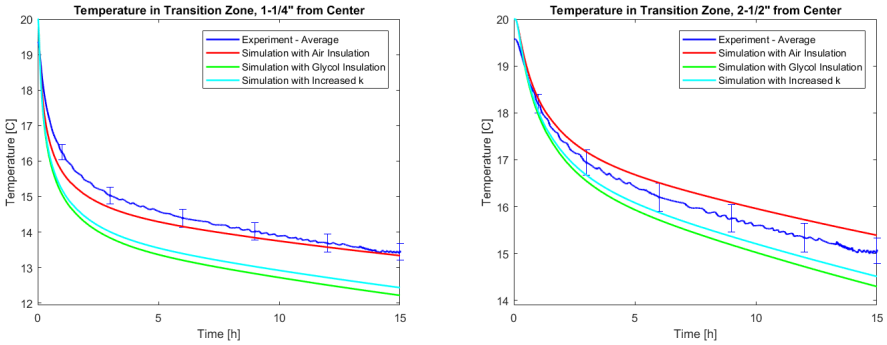

Figure 4.8: Unfrozen Sand Temperatures in Transition Zone

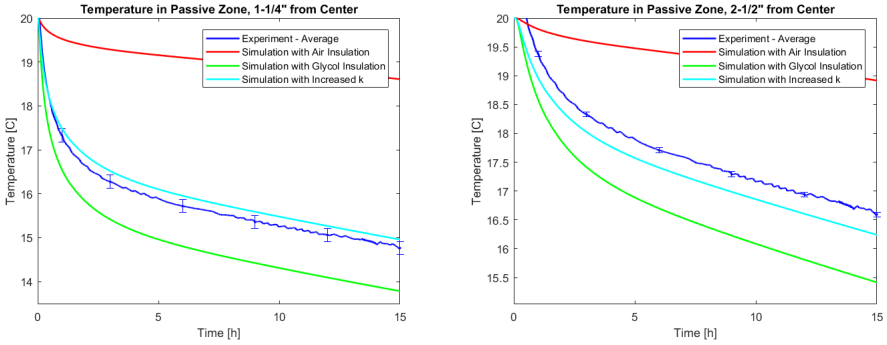

Figure 4.9: Unfrozen Sand Temperatures in Passive Zone

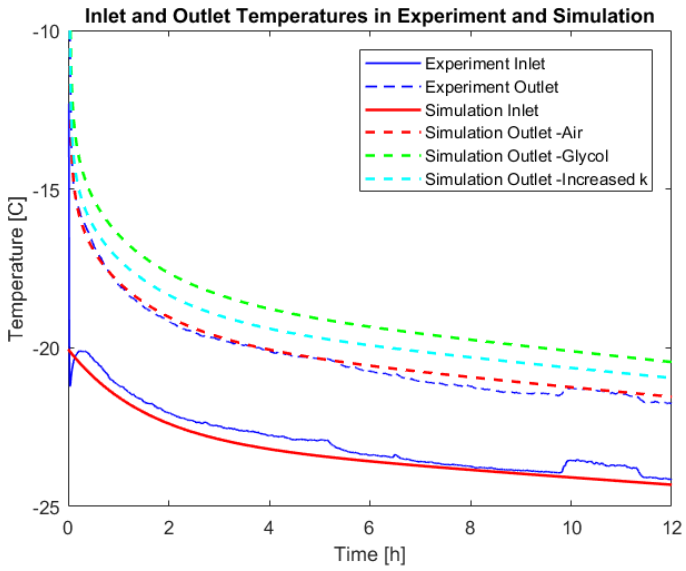

Figure 4.10: Inlet and Outlet Temperature in Frozen Conditions

Coolant Temperatures

Similar to previously, the numerical model uses a curve-fit of the recorded inlet temperature and flow rate for its boundary condition, as seen in Figure 4.10. The simulated outlet temperature fits the experimental data when air is used in the insulation, indicating the model's energy balance is correct.

Sand Temperatures

Similarly to the unfrozen regime, the low temperature trials have significant discrepancies in the passive zone, while the active and transition bear a similar fit. In this case, the best adjustment for air conductivity is $k = 0.15$ which corresponds to $Nu = 6.2$.

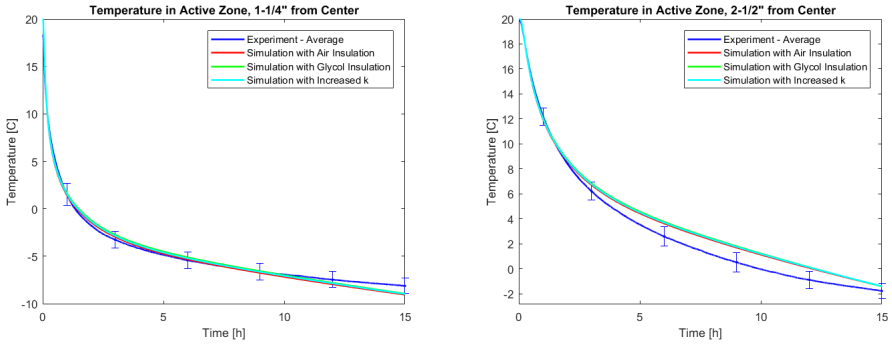

Figure 4.11: Frozen Sand Temperatures in Active Zone

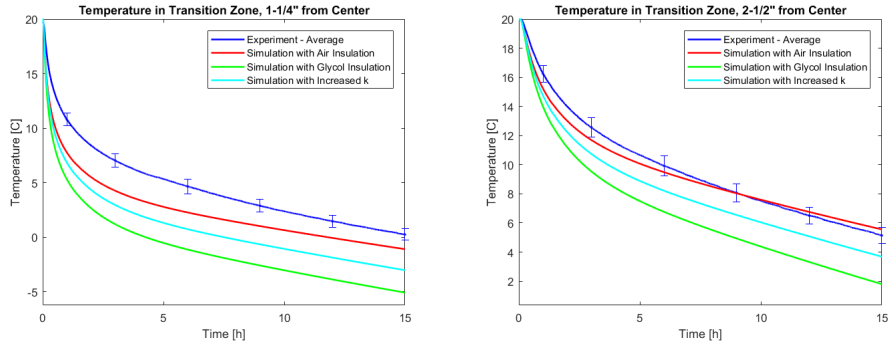

Figure 4.12: Frozen Sand Temperatures in Transition Zone

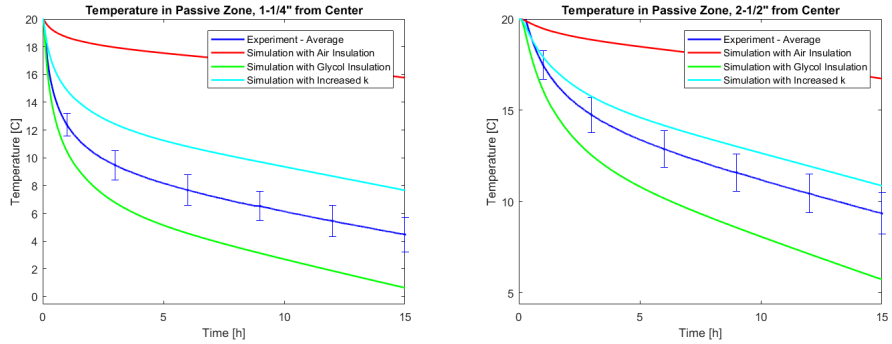

Figure 4.13: Frozen Sand Temperatures in Passive Zone

Chapter 5

Investigation of Eccentricity

One of the main purpose of this research topic is to find ways to improve the IBFT's efficiency. Translating to field requirements, this usually means faster freezing in the active zone and lower heat loss in the passive zone. One of the possible loss of thermal resistance in the passive zone is eccentricity. Depending on the field installations, the inner and outer insulation walls could come in contact, causing a short-circuit and adding direct conduction between pipes.

5.1 Numerical Model

The numerical model consists of a 1m segment of IBFT. Pipe dimensions (Figure 5.1) are based on field practices in Cigar Lake [31]. The meshing for the fully eccentric model required some adjustments: mesh elements close to the area of contact created large instabilities due to their large aspect ratio. To solve this issue, the contact area was enlarged slightly, and the mesh density was increased. In order to have a workable numerical model, only the IBFT was modeled; the ground region is ignored. A symmetry boundary condition helps reduce the mesh size to around 6.5 million elements when eccentric and 1 million otherwise. The set of equations described in Section 4.2.4 is the same one employed here.

The 25%, 50% and 75% eccentricity was calculated based on the gap between pipes. For these and the concentric models, the separating pipe and inner coolant were neglected as they were found to have a much lower impact than the outer coolant.

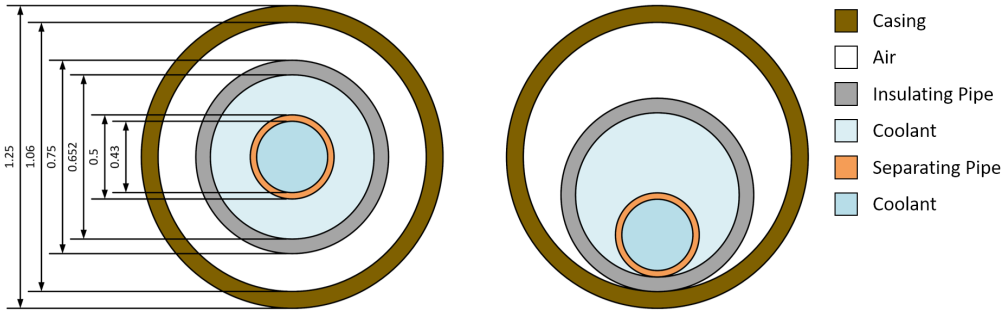

Figure 5.1: Geometry of Perfectly Concentric and Perfectly Eccentric IBFT

5.2 Results

5.2.1 Modes of Heat Transfer

Figure 5.2 shows the different modes of heat transfer depending on the eccentricity. For these results, ground and coolant are at 15 °C and -25°C respectively.

The most obvious feature of this graph is the importance of short-circuit on heat transfer in the passive zone. Direct contact between casing the inner pipe increases the heat loss by a whole order of magnitude when the inner PVC pipe is in contact with the outer casing, and three times that when the inner pipes is metallic.

It should be noted that due to the geometric simplification of Section 5.1 the coolant in the annulus does not come in direct contact with the short-circuit area. As may be seen in Figure 5.3, only the separating pipe made of PVC or steel has direct conduction. In other words, this model overpredicts the contribution of the short circuit while underpredicting the convection. This is an important distinction since field applications usually have the inflow in the inner pipe and the coldest temperate will be found there

Between 0% and 75% eccentricity, conduction increases while convection decreases. The analytical equation ($q = k\Delta T/L$) can explain conduction: eccentricity reduces the specific length on one side while increasing it on the other. Since $Q \propto 1/L$ the effect of the decrease is more significant than that of the increased length. For convection, the greater heat transfer is associated with larger temperature gradients in the air. This is correlated to an increase in buoyancy forces, and thus greater convective heat transfer.

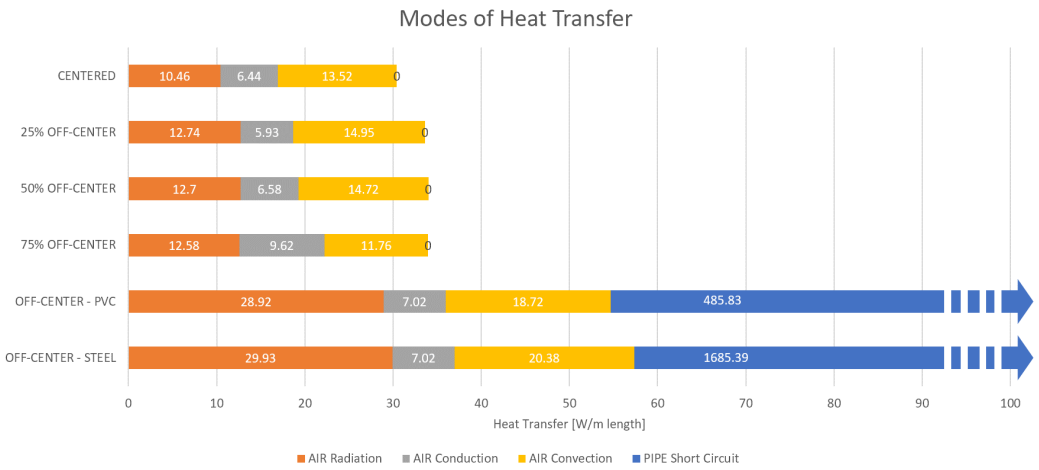

Figure 5.2: Modes of Heat Transfer in Concentric and Eccentric IBFT. Some values are cut off for clarity

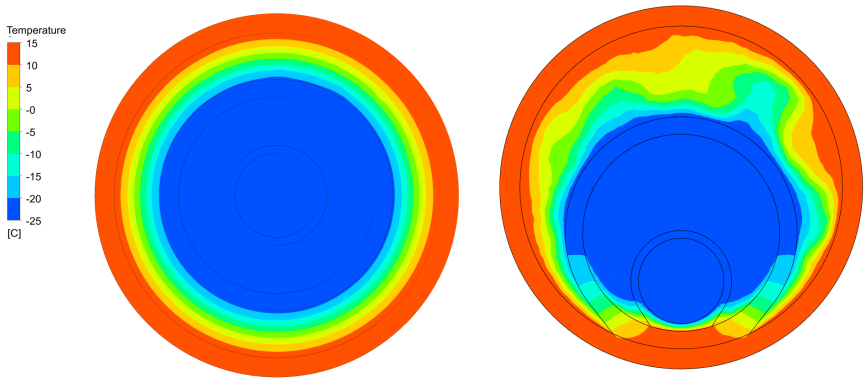

Figure 5.3: Temperature Profile in Concentric and Eccentric Configurations The inner pipe here is made of PVC

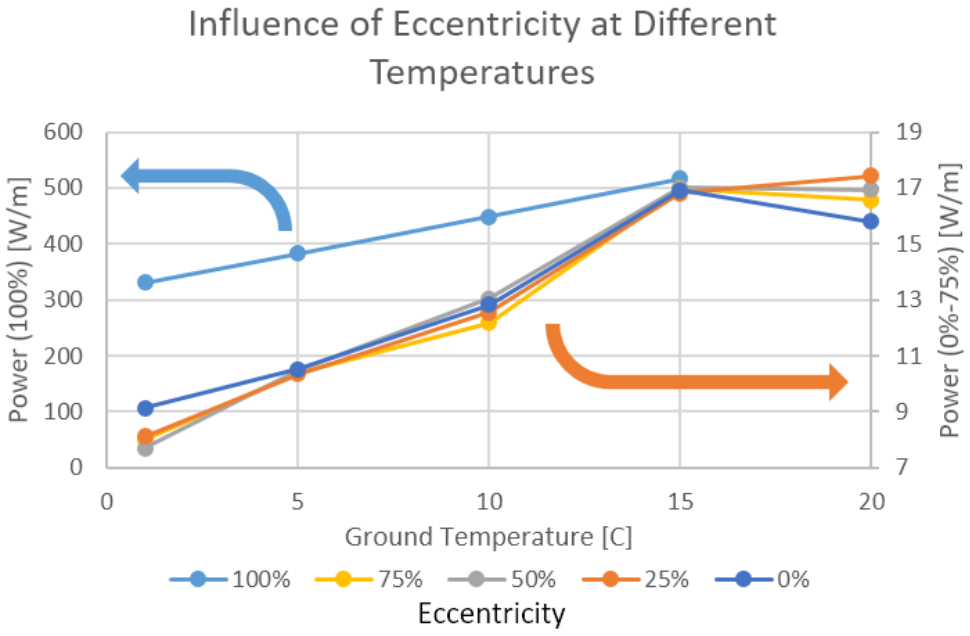

Figure 5.4: Effect of eccentricity at different temperatures

5.2.2 Influence of Temperature

One major shortcoming of the precious analysis is the assumption of fixed temperature boundary condition. In reality, a higher heat flow will lead to a lower ground temperature, which will gradually decrease the heat flow. To circumvent this issue, a parametric study is performed on the ground temperature. A constant coolant inlet temperature of -25°C will be assumed similar to the previous section.

The results presented in Figure 5.4 show that temperature affects the perfectly eccentric scenario in a linear fashion while the other cases have an almost asymptotic curve. This is no surprise: the short circuit is in the conduction regime and has a linear relationship with ΔT. The other scenarios have a significant portion of convection as mode of heat transfer, which is non-linear.

Chapter 6

Summary and Conclusion

A laboratory-scale model of an insulated bayonet tube was built and fitted with instrumentation. The thermal properties of the different materials used are measured in the laboratory. Thermocouples are installed at the coolant inlet and outlet and in the sand on three levels corresponding to the active, passive and transition zone. The tank is insulated to ensure no external conditions affect the results. A chiller and pump provide a constant ethylene glycol flow. A custom LabVIEW controls the flowrate and records the thermocouple readings. The readings of the different thermocouples are shown to provide repeatable results.

A numerical model of natural convection in a closed annulus is built in ANSYS and validated against literature. It is shown that the end caps of the annulus can strongly affect the flow patterns of the air. Another different numerical model is created with the geometry of the laboratory scale experiment. The air insulation uses the same setup as the natural convection model. Coolant outlet temperature matched closely the experimental results. Active and transition zone were also easily validated. However, the passive zone would have required an unrealistic Nusselt number of 9.3 to match the results. The reason the natural convection model in this case did not validate might be due to the drastic change in radius ratio. Further experimental studies on this topic are recommended to determine if this behavior is due to experimental or numerical inaccuracies. Another possible explanation for the discrepancy between numerical and experimental models is improper construction of the laboratory-scale AGF pipe. This could mean, for example that the pipe is off-centered, but the author believes this is unlikely.

A final model of the passive zone is used to demonstrate eccentricity

can greatly reduce the performance of air gap insulation in AGF systems. Conductive short-circuit between inner pipes and outer casing can increase the heat loss in a passive zone by a whole order of magnitude. The presence of a short circuit also significantly increases the heat transfer in the air region. However, as long as there is no contact, the effect of eccentricity is minimal. This behavior can be observed at every temperature.

Bibliography

[1] J.S. Harris. *Ground Freezing in Practice*. Heron Quay, London: Thomas Telford Services, 1995.

[2] Brian B Looney et al. *Independent technical support for the frozen soil barrier installation and operation at the Fukushima Daiichi Nuclear Power Station (F1 Site)*. Tech. rep. Savannah River Site (SRS), Aiken, SC (United States), 2015.

[3] P Bruneton. "Geological environment of the Cigar Lake uranium deposit". In: *Canadian Journal of Earth Sciences* 30.4 (1993), pp. 653–673.

[4] Megan Rose Roworth. "Understanding the effect of freezing on rock mass behaviour as applied to the Cigar Lake mining method". PhD thesis. University of British Columbia, 2013.

[5] T Johansson. "Artificial ground freezing in clayey soils". PhD thesis. Ph. D. Thesis, 2009.

[6] Seyed Ali Ghoreishi Madiseh. "Numerical and Experimental Study of Geothermal Energy Extraction from Underground Mines". PhD thesis. McGill University Libraries, 2014.

[7] Oistein Johansen. *Thermal conductivity of soils*. Tech. rep. Cold Regions Research and Engineering Lab Hanover NH, 1977.

[8] W.M.J.H. Woodside and J.H. Messmer. "Thermal conductivity of porous media. I. Unconsolidated sands". In: *Journal of applied physics* 32.9 (1961), pp. 1688–1699.

[9] Daniel A. de Vries. "Thermal properties of soils". In: *Physics of plant environment* (1963).

[10] Omar T Farouki. "The thermal properties of soils in cold regions". In: *Cold Regions Science and Technology* 5.1 (1981), pp. 67–75.

[11] Vlodek R Tarnawski and Wey H Leong. "A series-parallel model for estimating the thermal conductivity of unsaturated soils". In: *International Journal of Thermophysics* (2012), pp. 1–28.

[12] Vlodek R Tarnawski and Bernhard Wagner. "Modeling the thermal conductivity of frozen soils". In: *Cold regions science and technology* 22.1 (1993), pp. 19–31.

[13] Jean Côté and Jean-Marie Konrad. "A generalized thermal conductivity model for soils and construction materials". In: *Canadian Geotechnical Journal* 42.2 (2005), pp. 443–458.

[14] "A new method to model the thermal conductivity of soil–rock media in cold regions: An example from permafrost regions tunnel". In: *Cold Regions Science and Technology* 95 (2013), pp. 11 –18.

[15] Zhen Liu, Ye Sun, and Xiong Bill Yu. "Theoretical basis for modeling porous geomaterials under frost actions: A review". In: *Soil Science Society of America Journal* 76.2 (2012), pp. 313–330.

[16] Qian Li, Shufen Sun, and Yongkang Xue. "Analyses and development of a hierarchy of frozen soil models for cold region study". In: *Journal of Geophysical Research: Atmospheres* 115.D3 ().

[17] Barret L Kurylyk and Kunio Watanabe. "The mathematical representation of freezing and thawing processes in variably-saturated, non-deformable soils". In: *Advances in Water Resources* 60 (2013), pp. 160–177.

[18] "Thermal and Rheological Computations for Artificially Frozen Ground Construction". In: *Ground Freezing*. Ed. by HANS L. JESSBERGER. Vol. 26. Developments in Geotechnical Engineering. Elsevier, 1979, pp. 311 –337.

[19] "Numerical interpretation of temperature distributions from three ground freezing applications in urban tunnelling". In: *Tunnelling and Underground Space Technology* 28 (2012), pp. 57 –69.

[20] GP Newman and D Maishman. "Underground Freezing at a High Grade Uranium Mine". In: *Proceedings: International Symposium on Ground Freezing and Frost Action in Soils. Louvain-la-Neuve, Belgium.* 2000.

[21] "The aftermath of the Fukushima nuclear accident: Measures to contain groundwater contamination". In: *Science of The Total Environment* 547 (2016), pp. 261 –268.

[22] SRK Consulting. *Giant Mine Remediation Project Team Department of Indian Affairs and Northern Development*. Tech. rep. Yellowknife, NWT: Indian and Northern Affairs Canada Giant Mine Remediation Project, 2007.

[23] Herbert Victor. *Die Frostausbreitung beim künstlichen Gefrieren von Böden unter dem Einfluss strömenden Grundwassers*. Vol. 42. Univ., Inst. f. Bodenmechanik u. Felsmechanik, 1969.

[24] G Comini. "Seepage and heat flow in soil freezing". In: *Journal of Heat Transfer* 104 (1982), p. 323.

[25] E Pimentel, A Sres, and G Anagnostou. "Modelling of ground freezing in tunnelling". In: *Underground Space-the 4th Dimension of Metropolises, ITA and World Tunnel Congress, Prague*. 2007, pp. 331–336.

[26] Giancarlo Gioda, Livio Locatelli, and Francesco Gallavresi. "A numerical and experimental study of the artificial freezing of sand". In: *Canadian geotechnical journal* 31.1 (1993), pp. 1–11.

[27] Antonin Fabbri et al. "Investigation of water to ice phase change in porous media by ultrasonic and dielectric measurements". In: *Journal of Cold Regions Engineering* 23.2 (2009), pp. 69–90.

[28] E Pimentel, A Sres, and G Anagnostou. "Large-scale laboratory tests on artificial ground freezing under seepage-flow conditions". In: *Geotechnique* 62.3 (2012), p. 227.

[29] Wolfgang Ständer. *Mathematische Ansätze zur Berechnung der Frostausbreitung in ruhendem Grundwasser im Vergleich zu Modelluntersuchungen für verschiedene Gefrierrohranordnungen im Schactund Grundbau*. 28. Technische Hochschule Fridericiana, Institut für Bodenmechanik und Felsmechanik, 1967.

[30] Greg P Newman. "Case study: thermal analysis of artificial ground freezing at the McArthur river uranium mine". In: *Geotechnical News Vancouver* 21.2 (2003), pp. 60–62.

[31] Manon Vitel et al. "Thermo-hydraulic modeling of artificial ground freezing: Application to an underground mine in fractured sandstone". In: *Computers and Geotechnics* 75 (2016), pp. 80–92.

[32] "Modeling heat transfer between a freeze pipe and the surrounding ground during artificial ground freezing activities". In: *Computers and Geotechnics* 63 (2015), pp. 99 –111.

[33] G De Vahl Davis and RW Thomas. "Natural convection between concentric vertical cylinders". In: *The Physics of Fluids* 12.12 (1969), pp. II–198.

[34] M Keyhani, FA Kulacki, and RN Christensen. "Free convection in a vertical annulus with constant heat flux on the inner wall". In: *Journal of Heat Transfer* 105.3 (1983), pp. 454–459.

[35] RW Thomas and Graham de Vahl Davis. *Natural convection in annular and rectangular cavities. A numerical study.* Tech. rep. Univ. of New South Wales, Kensington, Australia, 1970.

[36] PD Weidman and G Mehrdadtehranfar. "Instability of natural convection in a tall vertical annulus". In: *The Physics of fluids* 28.3 (1985), pp. 776–787.

[37] Wei Qi and Yang Shiming. "Experimental study of natural convection heat transfer of air layers in vertical annuli under high Rayleigh number conditions". In: *Heat Transfer—Asian Research* 28.1 (1999), pp. 50–57.

[38] M Alipour, R Hosseini, and A Rezania. "Radius ratio effects on natural heat transfer in concentric annulus". In: *Experimental Thermal and Fluid Science* 49 (2013), pp. 135–140.

[39] R Hosseini et al. "Natural convection heat transfer from a long heated vertical cylinder to an adjacent air gap of concentric and eccentric conditions". In: *Heat and Mass Transfer* 48.1 (2012), pp. 55–60.

[40] N Sheriff. "Experimental investigation of natural convection in single and multiple vertical annuli with high pressure carbon dioxide." In: *Proceedings of the Third International Heat Transfer Conference, Chicago, Illinois*. United Kingdom Atomic Energy Authority, Risley, Eng. 1967, pp. 132–138.

[41] Inn G Choi and Seppo A Korpela. "Stability of the conduction regime of natural convection in a tall vertical annulus". In: *Journal of Fluid Mechanics* 99.4 (1980), pp. 725–738.

[42] GB McFadden et al. "Asymmetric instabilities in buoyancy-driven flow in a tall vertical annulus". In: *The Physics of fluids* 27.6 (1984), pp. 1359–1361.

[43] Ranganathan Kumar and MA Kalam. "Laminar thermal convection between vertical coaxial isothermal cylinders". In: *International journal of heat and mass transfer* 34.2 (1991), pp. 513–524.

[44] Sheng Chen et al. "Natural convection and entropy generation in a vertically concentric annular space". In: *International Journal of Thermal Sciences* 49.12 (2010), pp. 2439–2452.

[45] R Bhushan et al. "Correlation equations for free convection in a vertical annulus with constant heat flux on the inner wall". In: *ASME Journal of Heat Transfer* 105 (1983), pp. 910–912.

[46] *GLACIER Refrigerated Bath Circulator Manual*. English. Thermo Fisher Scientific. 2015.

[47] Mark A. Finlayson. *Brooks Oval Flowmeters Installation and Operaiton Manual*. English. Brooks Instrument. 2008.

[48] GK Batchelor. "Heat transfer by free convection across a closed cavity between vertical boundaries at different temperatures". In: *Quarterly of Applied Mathematics* 12.3 (1954), pp. 209–233.